

CROSS-POPULATION AMPLITUDE COUPLING IN HIGH-DIMENSIONAL OSCILLATORY NEURAL TIME SERIES

BY HEEJONG BONG¹, VALÉRIE VENTURA^{1,2,5}, ERIC YTTRI^{3,5},
MATTHEW A. SMITH^{4,5} AND ROBERT E. KASS^{1,2,5,*}

¹Department of Statistics and Data Sciences, Carnegie Mellon University, *kass@stat.cmu.edu

²Machine Learning Department, Carnegie Mellon University,

³Department of Biological Sciences, Carnegie Mellon University,

⁴Department of Biomedical Engineering, Carnegie Mellon University,

⁵Neuroscience Institute, Carnegie Mellon University,

An important outstanding problem in analysis of neural data is to characterize interactions across brain regions from high-dimensional multiple-electrode recordings during a behavioral experiment. A leading theory, based on a considerable body of research, is that oscillations represent coordinated activity across populations of neurons. We sought to quantify time-varying covariation of oscillatory amplitudes across two brain regions, during a memory task, based on neural potentials recorded from 96 electrodes in each region. We extended probabilistic Canonical Correlation Analysis (CCA) to the time series setting, which provides a new interpretation of multiset CCA based on cross-correlation of latent time series. Because the latent time series covariance matrix is high-dimensional, we assumed sparsity of partial correlations within a range of possible interesting time series lead-lag effects to derive procedures for estimation and inference. We found the resulting methodology to perform well in realistic settings, and we applied it to data recorded from prefrontal cortex and visual area V4 to produce results that are highly plausible based on existing literature.

1. Introduction. Contemporary technologies for recording neural activity can produce multiple time series in each of two or more brain regions simultaneously (e.g., Jun et al., 2017; Steinmetz et al., 2018), enabling identification of cross-regional interactions relevant to cognitive processes that support behavior. One such process, which is crucial for humans and other mammals, is the purposeful short-term storage of information known as “working memory” (Miller, Lundqvist and Bastos, 2018; Schmidt et al., 2019). During a variety of experimental working memory tasks, strong neural oscillations in the beta range (16-30 Hz) have been observed, leading to the proposal that beta oscillations serve to coordinate activity across regions (Miller, Lundqvist and Bastos, 2018). To identify coordinated oscillatory activity, many statistical methods based on coherence, or phase coupling, have been developed, studied, and applied Ombao and Pinto (2022); Klein et al. (2020). As shown in Fig. 1, however, oscillatory amplitudes (amplitude envelopes) also vary substantially and may well exhibit statistical dependence across regions. In this paper, we develop methods to analyze the amplitude envelopes of 96 oscillatory time series recorded simultaneously from each of two brain regions during a working memory task. Our goal is to identify any tendency of the amplitudes in the two high-dimensional series to vary together, across the two regions, and to further identify the time during the experimental task when this statistical dependence occurs. Such coupling of oscillatory amplitudes would indicate coordinated neural activity.

Keywords and phrases: Latent factor model, High-dimensional time-series, Multiset CCA, Cross-region dynamic connectivity.

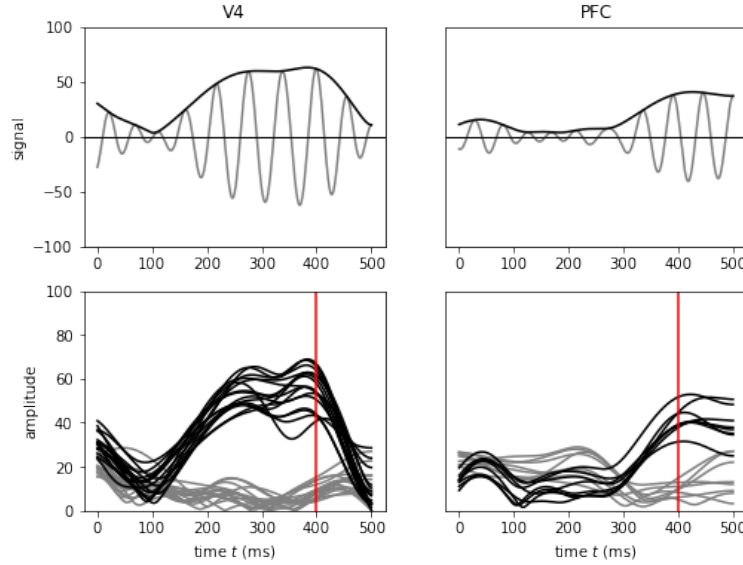


Fig 1: Bandpass-filtered LFP amplitude envelopes. The top panels display beta-range filtered LFPs (gray) together with their amplitude envelopes (black) from a pair of electrodes in V4 (left) and PFC (right) on a single trial, during the delay period of a working memory task. (The filtering is described in Section 3.1.) The bottom panels display amplitude envelopes of active electrodes in the two brain regions for two trials, those for one trial in black and those for the other trial in gray. The beta amplitude envelopes show a consistent temporal pattern within each region, for both trials, and, at 400 ms (red vertical line), the two groups of amplitude envelopes from the two brain regions illustrate correlated behavior across the two trials in the sense that the black amplitude curves for the first trial are elevated, compared with the gray for the second trial, in both V4 and PFC. This correlation, however, varies across time.

The data we use to motivate this work are local field potentials (LFPs), which measure bulk neural activity in the vicinity of electrodes inserted into brain tissue *in vivo* (Buzsáki, Anastassiou and Koch, 2012; Pesaran et al., 2018), recorded from prefrontal cortex (PFC) and visual area V4 during many repetitions of a working memory task. PFC is generally considered to exert control aimed at areas involved in perceptual processing (Miller and Cohen, 2001), such as V4, which is active during the retention of higher order visual information (e.g. color and shape) and attention to visual objects (Orban, 2008; Fries et al., 2001). Strong beta oscillations occur in both areas during visual working memory tasks (Sarnthein et al., 1998; Liebe et al., 2012).

LFPs offer millisecond temporal precision, and are relatively precise spatially, as well. However, each set of 96 LFP time series, measuring activity within a large population of neurons that make up that region of the brain, exhibits substantial spatial correlation. This suggests reducing the data with the objective of capturing cross-region dependence. If we were to consider a single time point we would have repeated pairs of 96-dimensional observations and an obvious statistical assessment of dependence would be canonical correlation analysis (CCA). Here we use the latent variable formulation of CCA known as probabilistic CCA (pCCA), and extend it to the time series setting, as depicted in Fig. 2b. In the extended model described in Section 2.2, each of the two high-dimensional time series is driven by a latent univariate time series, with the correlation between the two latent time series representing the statistical dependence we seek to identify (see Fig. 3). Theorem 2.3 demonstrates that the maximum likelihood estimate for this model is equivalent to that derived from multiset

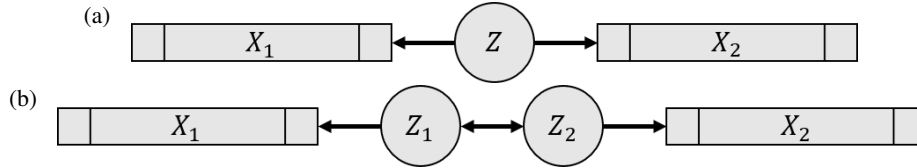


Fig 2: **Graphical representation of pCCA models.** (a) Model of [Bach and Jordan \(2005\)](#), where X_1 and X_2 are random vectors and Z is a random variable. (b) A variation on (a) that facilitates the extension to the case when X_1 and X_2 are multivariate time series and (Z_1, Z_2) is a bivariate time series.

CCA, as introduced by [Kettenring \(1971\)](#). The model-based framework retains generality in the specification of covariation while clarifying application of methods for high-dimensional inference.

A related latent variable method, Gaussian Process Factor Analysis (GPFA, [Gokcen et al., 2021](#); [Lakshmanan et al., 2015](#); [Semedo et al., 2020](#); [Yu et al., 2009](#)), is popular in the neuroscience literature. As the name implies, GPFA assumes the latent time series have a low-dimensional Gaussian process structure defining their covariance matrix. Here, we instead leave the latent covariance matrix unspecified so that our estimate of the correlation matrix has maximal flexibility. This approach provides a partial-correlation graph interpretation of the cross-regional dependence. Because the graphical model describing general, non-stationary dependence is high-dimensional, we resort to sparse estimation methods, calling the method *Latent Dynamic analysis via Sparse banded graphs* (LaDynS).

In Section 2, after defining the model and proving that it produces a time series generalization of CCA, we give details of the fitting procedure and discuss inference using clustered contiguous significant association based on a de-biased estimate of the precision matrix ([Jankova et al., 2015](#)) together with control of false discovery rate ([Benjamini and Hochberg, 1995](#)). We also use a state-space formulation to impose a local stationarity assumption ([Ombao and Pinto, 2022](#)), pointing out how this can produce a time-varying latent Granger causality assessment. Simulations in Section 3 show that our implementation of LaDynS is able to correctly identify the timing of interactions when applied to artificial data designed to be similar to those we analyzed. The simulations support data-analytic results presented in Section 4, which show significant cross-regional dependence at roughly 400 ms after presentation of the stimulus (see Fig. 10). This timing coincides with the delay in visual cortical response seen during perception of a stimulus in mice ([Chen et al., 2022](#)), humans ([Del Cul, Baillet and Dehaene, 2007](#); [Yang et al., 2019](#)), and macaques ([Supèr, Spekreijse and Lamme, 2001](#)). The results reinforce the idea that PFC and V4 are involved, together, in working memory. We add discussion in Section 5.

2. Methods. We begin by reviewing and reformulating probabilistic CCA (pCCA) in Section 2.1, which we then generalize to time series in Section 2.2 to yield a dynamic version of pCCA. Theorem 2.3 establishes an equivalence between the GENVAR version of multi-set CCA ([Kettenring, 1971](#)) and maximum likelihood applied to our dynamic pCCA. We define the LaDynS model based on the loglikelihood function in Definition 2.4. We go over choice of regularization parameters in Section 2.3.1 and the fitting algorithm in Section 2.3.2. We discuss statistical inference in Section 2.4.

2.1. Probabilistic CCA for two random vectors. Given two random vectors $X_1 \in \mathbb{R}^{d_1}$ and $X_2 \in \mathbb{R}^{d_2}$, canonical correlation analysis (CCA) ([Hotelling, 1992](#)) finds the sets of

weights $w_1 \in \mathbb{R}^{d_1}$ and $w_2 \in \mathbb{R}^{d_2}$ that maximize Pearson's correlation between linear combinations $w_1^\top X_1$ and $w_2^\top X_2$. This can be rewritten as

$$(1) \quad \sigma_{cc} = \max_{w_k, k=1,2: w_k^\top \Sigma_{kk} w_k = 1} \left| w_1^\top \Sigma_{12} w_2 \right|,$$

where $\Sigma_{kk} = \text{Var}(X_k)$ is the covariance matrix of X_k , $k = 1, 2$, and $\Sigma_{12} = \text{Cov}(X_1, X_2)$ the cross-covariance matrix between X_1 and X_2 . The sample estimator $\hat{\sigma}_{cc}$ is obtained by replacing Σ_{kk} and Σ_{12} with their sample analogs $\bar{\Sigma}_{kk}$ and $\bar{\Sigma}_{12}$ respectively. The maximizing weights \hat{w}_k and linear combinations $\hat{Z}_k = \hat{w}_k^\top X_k$ are referred to as the canonical weights and canonical variables, respectively.

Probabilistic CCA assumes that X_1 and X_2 are driven by a common one dimensional latent variable Z :

$$(2) \quad \begin{aligned} X_k | Z &= \mu_k + Z \cdot \beta_k + \epsilon_k, \quad k = 1, 2, \\ Z &\sim N(0, 1), \end{aligned}$$

where $\mu_k \in \mathbb{R}^{d_k}$ and $\beta_k \in \mathbb{R}^{d_k}$ are mean vectors and factor loadings, respectively, and $\epsilon_k \stackrel{\text{indep}}{\sim} \text{MVN}(0, \Phi_k)$ (Bach and Jordan, 2005). Fig. 2a depicts the dependence of X_1 and X_2 on Z . The parameters in Eqs. (1) and (2) relate as follows:

THEOREM 2.1 (Bach and Jordan, 2005, Theorem 2). *The maximum likelihood estimators (MLEs) $(\hat{\beta}_1, \hat{\beta}_2)$ in Eq. (2) based on N observed vector pairs $\{X_{1[n]}, X_{2[n]}\}_{n=1,2,\dots,N}$ are equivalent to the CCA solution $(\hat{w}_1, \hat{w}_2, \hat{\sigma}_{cc})$ in Eq. (1) according to:*

$$(3) \quad \hat{\beta}_k = \bar{\Sigma}_{kk} \hat{w}_k m_k, \text{ where } m_1 m_2 = \hat{\sigma}_{cc} \text{ and } |m_k| \leq 1, \quad k = 1, 2.$$

Theorem 2.1 proves that the original CCA setting and the generative pCCA model both yield the same estimate of σ_{cc} .

Next, we introduce an alternative pCCA extension that assigns distinct latent variables for X_1 and X_2 , as depicted in Fig. 2b. Specifically, we assume that

$$(4) \quad X_k | Z_k = \mu_k + Z_k \cdot \beta_k + \epsilon_k$$

where $\mu_k \in \mathbb{R}^{d_k}$, $\beta_k \in \mathbb{R}^{d_k}$ and $\epsilon_k \stackrel{\text{indep}}{\sim} \text{MVN}(0, \Phi_k)$ are defined as in Eq. (2), and (Z_1, Z_2) are bivariate normally distributed:

$$(5) \quad \begin{pmatrix} Z_1 \\ Z_2 \end{pmatrix} \sim \text{MVN} \left(\begin{pmatrix} 0 \\ 0 \end{pmatrix}, \begin{pmatrix} 1 & \sigma_{12} \\ \sigma_{12} & 1 \end{pmatrix} \right).$$

We now state an equivalence similar to Theorem 2.1 between the original CCA and the alternative pCCA model.

THEOREM 2.2. *The MLEs $(\hat{\beta}_1, \hat{\beta}_2, \hat{\sigma}_{12})$ in Eqs. (4) and (5) based on N observed vector pairs $\{X_{1,[n]}, X_{2,[n]}\}_{n=1,2,\dots,N}$ are equivalent to the CCA solution $(\hat{w}_1, \hat{w}_2, \hat{\sigma}_{cc})$ according to:*

$$(6) \quad \hat{\beta}_k = \bar{\Sigma}_{kk} \hat{w}_k m_k, \text{ where } m_1 m_2 \hat{\sigma}_{12} = \hat{\sigma}_{cc} \text{ and } |m_k| \leq 1, \quad k = 1, 2.$$

Theorem 2.2 is a corollary of Theorem 2.3. The latter extends the former to the time series case. In practice we take $m_1 = m_2 = 1$ out of all possible solutions, because then $Z_k | X_k = \hat{w}_k^\top X_k$ is the canonical variable almost surely, as proven in Theorem 2.3, and $\sigma_{12} = \text{Cov}[Z_1, Z_2]$ equals the canonical correlation σ_{cc} . This means that σ_{12} is an interpretable parameter, and one for which inference is simpler than for the canonical correlation

in the other model, because, in Eq. (2), $\widehat{\sigma}_{cc}$ is an indirect function of the maximum-likelihood parameter estimates (see Theorem 2.1). The interpretability property also persists when we extend model (5) to capture lagged association between two vector time series (see model (8)). Finally, the choice $m_1 = m_2 = 1$ implies that the MLEs $(\widehat{\beta}_1, \widehat{\beta}_2, \widehat{\sigma}_{12})$ do not depend on the Gaussian assumption in Eq. (4) (see Theorem 2.3), an assumption that is questionable if, for example, the X 's are positive variables like LFP power envelopes or discrete variables like spike counts.

2.2. Probabilistic CCA for two time series of random vectors . Suppose now that we are interested in the correlation dynamics between two times series of random vectors $X_1^{(t)} \in \mathbb{R}^{d_1}$ and $X_2^{(t)} \in \mathbb{R}^{d_2}$, $t = 1, 2, \dots, T$. For each time t , we use Eq. (4) to model the dependence of $X_k^{(t)}$ on its associated latent variable $Z_k^{(t)}$:

$$(7) \quad X_k^{(t)} | Z_k^{(t)} = \mu_k^{(t)} + \beta_k^{(t)} \cdot Z_k^{(t)} + \epsilon_k^{(t)}, \quad k = 1, 2,$$

where $\mu_k^{(t)}, \beta_k^{(t)}$ and $\epsilon_k^{(t)} \stackrel{\text{indep}}{\sim} \text{MVN}(0, \Phi_k^{(t)})$ are defined as in Eq. (4). Then for each t we could define a parameter $\sigma_{12}^{(t)}$ as in Eq. (5) to capture population-level association between $X_1^{(t)}$ and $X_2^{(t)}$ at t . But because we are also interested in lagged associations between $X_1^{(t)}$ and $X_2^{(s)}$ for $s \neq t$, we replace the bivariate model (5) for $Z_1^{(t)}$ and $Z_2^{(t)}$ for a given t by a global model for all $t = 1, \dots, T$:

$$(8) \quad \left(\left(Z_1^{(t)} \right)_{t=1, \dots, T}, \left(Z_2^{(t)} \right)_{t=1, \dots, T} \right)^\top \sim \text{MVN}(0, \Sigma), \quad \text{diag}(\Sigma) = \mathbf{1},$$

where Σ captures jointly all simultaneous and lagged associations within and between the two time series. Fig. 3a illustrates the dependence structure of this model. We decompose Σ and its inverse Ω as

$$(9) \quad \Sigma = \begin{pmatrix} \Sigma_{11} & \Sigma_{12} \\ \Sigma_{12}^\top & \Sigma_{22} \end{pmatrix} \quad \text{and} \quad \Omega = \begin{pmatrix} \Omega_{11} & \Omega_{12} \\ \Omega_{12}^\top & \Omega_{22} \end{pmatrix}$$

to highlight the auto-correlations Σ_{11} and Σ_{22} within and cross-correlations Σ_{12} between the time series, and denote by $\Sigma_{kl}^{(t,s)}$, $(t, s) \in [T]^2$, the elements of Σ_{kl} . Then $\Sigma_{12}^{(t,t)}$ for some fixed t has the same interpretation as σ_{12} in Eq. (2). Further, $-\Omega_{12}^{(t,s)} / \sqrt{\Omega_{11}^{(t,t)} \Omega_{22}^{(s,s)}}$ is the partial correlation between the two latent time series at times t and s . Thus, when an element of Ω_{12} is non-null, depicted by the red star in the expanded display in Fig. 3b, its coordinates (t, s) and distance $(t - s)$ from the diagonal indicate at what time in the trial a connectivity happens between two time series, and at what lead or lag, respectively. In our neuroscience application, they represent the timing of connections and direction of information flow between two brain regions.

Theorem 2.2 provided an equivalence between a non-distributional method (CCA) and its probabilistic representation (pCCA). We now derive a similar connection between the multiset generalization of CCA introduced by Kettenring (1971) and the dynamic pCCA model in Eqs. (7) and (8). Multiset CCA applied to $2T$ random vectors $\{X_1^{(t)}, X_2^{(t)} : t = 1, \dots, T\}$ finds weights $\{w_1^{(t)}, w_2^{(t)} : t = 1, \dots, T\}$ that maximize a notion of correlation among linear combinations $\{w_1^{(t)\top} X_1^{(t)}, w_2^{(t)\top} X_2^{(t)} : t = 1, \dots, T\}$. In particular, the GENVAR extension minimizes the generalized variance of these linear combinations, defined as the determinant of their correlation matrix (Wilks, 1932), which we refer to as the canonical correlation matrix:

$$(10) \quad \widehat{w}_1^{(1)}, \dots, \widehat{w}_2^{(T)} = \underset{w_1^{(1)}, \dots, w_2^{(T)}}{\text{argmin}} \det \left(\overline{\text{Var}} \left[\left(w_1^{(t)\top} X_1^{(t)} \right)_{t=1, \dots, T}, \left(w_2^{(t)\top} X_2^{(t)} \right)_{t=1, \dots, T} \right] \right)$$

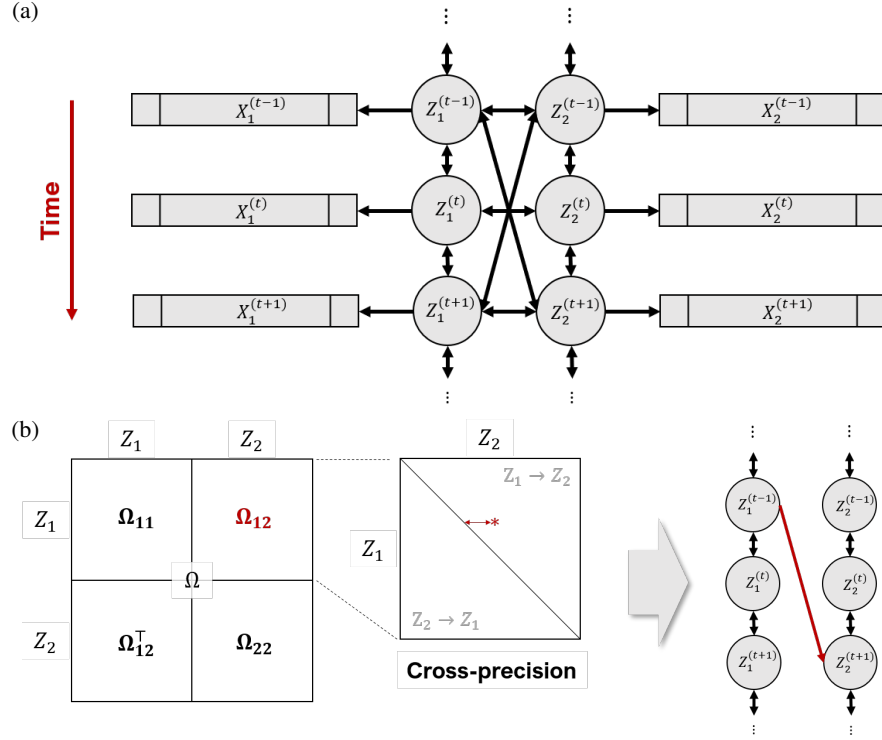


Fig 3: **Extended pCCA model for two multivariate time series** $X_1^{(t)}$ and $X_2^{(s)}$, $t, s = 1, \dots, T$. **(a)** Dynamic associations between vectors $X_1^{(t)}$ and $X_2^{(s)}$ are summarized by the dynamic associations between their associated 1-dimensional latent variables $Z_1^{(t)}$ and $Z_2^{(s)}$ represented by their cross-precision matrix Ω_{12} . **(b)** When a significant cross-precision entry is identified, e.g., the red star in the expanded view of Ω_{12} , its coordinates and distance from the diagonal indicate at what time in the experiment connectivity between two brain areas occurs, and at what lead or lag. Here the red star is in the upper diagonal of Ω_{12} , which means that, at this particular time, region 1 leads region 2, or $Z_1 \rightarrow Z_2$ in short (a non-zero entry in the lower diagonal would mean $Z_2 \rightarrow Z_1$). We represent this association by the red arrow on the right-most plot, with a lag of two units of time for illustration.

where $\overline{\text{Var}}$ denotes the sample variance-covariance matrix and the weights $w_k^{(t)}$ are scaled so that every diagonal entry of the matrix is 1. The proof is in Appendix A.

THEOREM 2.3. Suppose that $\hat{\beta}_k^{(t)}$, $k = 1, 2$, $t = 1, \dots, T$, and $\hat{\Sigma}$ are the MLE in Eqs. (7) and (8) based on N observed pairs of vector time series $\{X_{1[n]}^{(t)}, X_{2[n]}^{(t)} : t = 1, \dots, T\}$, $n = 1, \dots, N$. Then, they are equivalent to GENVAR multiset CCA solution according to:

$$(11) \quad \hat{\beta}_k^{(t)} = \overline{\text{Var}}[X_k^{(t)}] \hat{w}_k^{(t)} m_k^{(t)} \text{ and } \hat{\Sigma}_{kl}^{(t,s)} = \begin{cases} 1, & k = l \text{ and } t = s, \\ \overline{\text{Var}}[\hat{Z}_k^{(t)}, \hat{Z}_l^{(s)}], & \text{elsewhere,} \end{cases}$$

where the canonical variable is

$$(12) \quad \hat{Z}_k^{(t)} = \hat{w}_k^{(t)\top} X_k^{(t)} = \frac{1}{m_k^{(t)}} \hat{\beta}_k^{(t)\top} \overline{\text{Var}}^{-1}[X_k^{(t)}] X_k^{(t)},$$

and $|m_k^{(t)}| \leq 1$ for $k = 1, 2$ and $t \in [T]$. Furthermore, if all $m_k^{(t)} = 1$, then the MLE minimizes

$$(13) \quad \log \det(\Sigma) + \text{tr}(\Sigma^{-1} \bar{\Sigma}),$$

where $\bar{\Sigma} = \overline{\text{Var}} \left[\left(\beta_1^{(t)\top} \overline{\text{Var}}^{-1} [X_1^{(t)}] X_1^{(t)} \right)_{t=1, \dots, T}, \left(\beta_2^{(t)\top} \overline{\text{Var}}^{-1} [X_2^{(t)}] X_2^{(t)} \right)_{t=1, \dots, T} \right]$, with β_1 and β_2 scaled such that $\text{diag} \bar{\Sigma} = \mathbf{1}$.

Theorem 2.2 is a corollary of Theorem 2.3. See the end of Appendix A.

Notice that Eq. (13) does not involve any component of Eq. (7) so the MLEs do not depend on the Gaussian assumption of $X_k^{(t)}$ given $Z_k^{(t)}$. This is confirmed by simulation in Section 3. The MLEs do however depend on the Gaussian distribution in Eq. (8), but this assumption is more easily justifiable: the latent factors are the canonical variables $\hat{w}_k^{(t)\top} X_k^{(t)}$, which are weighted sums of the observations and thus likely to be close to Gaussian, based on a central limit theorem.

2.3. Latent Dynamic Analysis via Sparse Banded Graphs (LaDynS). Our goal is to estimate the association dynamics between two multivariate time series using the covariance matrix Σ of their associated latent time series in Eq. (13). However, the prohibitive number of parameters in Σ means its estimation is prone to errors, especially when T is large. We reduce their number by regularizing $\Omega = \Sigma^{-1}$ in Eq. (13), rewriting $\log \det(\Sigma) = \log \det(\Omega^{-1}) = -\log \det(\Omega)$, and assuming that Ω has the banded structure depicted in Fig. 4.

DEFINITION 2.4 (LaDynS). Given N simultaneously recorded pairs of multivariate time series $\{X_{1[n]}, X_{2[n]}\}_{n=1, \dots, N}$, and a $2T \times 2T$ sparsity matrix Λ with element $\Lambda_{kl}^{(t,s)}$ regularizing $|\Omega_{kl}^{(t,s)}|$, $k, l = 1, 2$, LaDynS finds weights $\{\hat{w}_k^{(t)}, t = 1, 2, \dots, T, k = 1, 2\}$ and precision matrix $\hat{\Omega}$ that minimize the penalized negative log-likelihood:

$$(14) \quad -\log \det(\Omega) + \text{tr}(\Omega \bar{\Sigma}) + \|\Lambda \odot \Omega\|_1,$$

where $\bar{\Sigma} = \overline{\text{Var}} \left[w_1^{(1)\top} X_1^{(1)}, \dots, w_2^{(T)\top} X_2^{(T)} \right]$ satisfies $\text{diag}(\bar{\Sigma}) = \mathbf{1}$, \odot denotes the Hadamard product operator such that $(A \odot B)_{ij} = A_{ij} \times B_{ij}$, $\|A\|_1 = \sum_{i,j} |A_{ij}|$, and

$$\Lambda_{kl}^{(t,s)} = \begin{cases} \lambda_{\text{cross}}, & k \neq l \text{ and } 0 < |t - s| \leq d_{\text{cross}}, \\ \lambda_{\text{auto}}, & k = l \text{ and } 0 < |t - s| \leq d_{\text{auto}}, \\ \lambda_{\text{diag}}, & t = s, \\ \infty, & \text{otherwise,} \end{cases}$$

which constrains auto-precision and cross-precision elements within a specified range.

In our neuroscience application, in particular, it is reasonable to assume that lead-lag relationships occur with delay less than temporal bandwidth d_{cross} , which can be determined by the maximal transmission time in synaptic connections between two brain regions under study. We thus set $\Lambda_{12}^{(t,s)} = \infty$ when $|t - s| > d_{\text{cross}}$ to force the corresponding cross-precision elements to zero and thus impose a banded structure on Ω_{12} . We apply sparsity constraint $\Lambda_{12}^{(t,s)} = \lambda_{\text{cross}} > 0$ on the remaining off-diagonals of Ω_{12} to focus our discovery on sparse dominant associations and reduce the effective parameter size. We proceed similarly with the auto-precision matrices Ω_{11} and Ω_{22} , using penalty λ_{auto} and temporal bandwidth d_{auto} . Unless domain knowledge is available, we recommend that d_{auto} be set to the largest significant

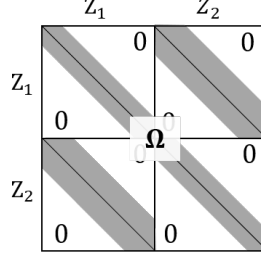


Fig 4: The elements of Ω_{kk} , $k = 1, 2$, and Ω_{12} are set to zero outside of the gray bands of widths $(1 + 2d_{\text{auto}})$ and $(1 + 2d_{\text{cross}})$, respectively.

auto-correlation across all observed time series $X_{k,i}^{(t)}$, $k = 1, 2$, $i = 1, \dots, N$, and impose no further sparsity ($\lambda_{\text{auto}} = 0$) unless there is reason to expect it.

Notice that to facilitate the choice of Λ , we grouped its elements into diagonal and off-diagonal elements and assigned the same penalties, λ_{cross} , $\lambda_{\text{auto}} = 0$ and λ_{diag} , within each group.

2.3.1. Choosing regularization parameters. In graphical LASSO (gLASSO) problems, where the aim is to recover correct partial correlation graphs, penalties are often chosen to minimize the predictive risk (Shao, 1993; Zou et al., 2007; Tibshirani et al., 2012). Our aim is different: only the partial cross-precision matrix Ω_{12} is of substantive interest, and because minimizing the predictive risk does not select models consistently (Shao, 1993; Zhu and Cribben, 2018) and may thus fail to retrieve non-zero elements of Ω_{12} , we choose instead a value of λ_{cross} that controls the number of false cross-precision discoveries. We proceed by permuting the observed time series in one brain region to create a synthetic dataset that contains no cross-region correlation, then applying LaDynS to that data for a range of values of λ_{cross} and recording the resulting number of significant partial correlation estimates, which are necessarily spurious. We use the smallest λ_{cross} that yields fewer false discoveries than a chosen threshold. We expect this regularization to make similarly few false discoveries on experimental data.

Finally, if $\hat{\Sigma}$ cannot be inverted, as is the case for the band-pass filtered experimental data we analyze in Sections 3 and 4, we penalize its diagonal by $\lambda_{\text{diag}} > 0$. We explain the specific calibration we used for the analyzed datasets in Section 3.2 and study the properties in Section 3.3.

2.3.2. Fitting LaDynS using coordinate descent. Eq. (14) is not a convex function of the weights and precision elements (although it is not impossible that it may be for some particular Σ) and its convex relaxation is unknown, so it is difficult to find its global minimum. The coordinate descent algorithm described below finds a minimum, possibly local since it may be sensitive to the choice of initial parameter values. See Appendix B.2 in the Supplementary Material.

Assuming that all canonical weights $w_k^{(t)}$ are fixed, Eq. (14) reduces to the gLASSO problem:

$$(15) \quad \underset{\Omega}{\operatorname{argmin}} -\log \det(\Omega) + \operatorname{tr}(\Omega \bar{\Sigma}) + \|\Lambda \odot \Omega\|_1,$$

which we can solve efficiently using a number of existing algorithms; here we use the P-gLASSO algorithm of Mazumder and Hastie (2012). Then assuming that all parameters are

fixed but a single weight $w_k^{(t)}$, Eq. (14) can be re-arranged as the linear problem:

$$(16) \quad \underset{w_k^{(t)}}{\operatorname{argmin}} \sum_{(l,s) \neq (k,t)} w_k^{(t)\top} \overline{\operatorname{Cov}} [X_k^{(t)}, X_l^{(s)}] w_l^{(s)} \Omega_{kl}^{(t,s)} \quad \text{s.t.} \quad w_k^{(t)\top} \overline{\operatorname{Var}} [X_k^{(t)}] w_k^{(t)} = 1,$$

for which an analytical solution is available. That is, our algorithm alternates between updating Ω and the weights $w_k^{(t)}$ until the objective function in Eq. (14) converges. Its computational cost is inexpensive: a single iteration on our cluster server (with 11 Intel(R) Xeon(R) CPU 2.90 GHz processors) took in average less than 0.8 seconds, applied to the experimental data in Section 4. A single fit on the same data took 47 iterations for around 33.57 seconds until the objective function converged at threshold 0.001. See Algorithm 1 in Appendix B.1 for details and Python package `ladyns` on github.com/HeejongBong/ladyns.

2.4. Inference for associations between two vector time series. Let $\hat{\Omega}$ and $\hat{w}_k^{(t)}$, $t = 1, \dots, T$, $k = 1, 2$, be the LaDynS estimates of canonical precision matrix and canonical weights, and $\bar{\Sigma} = \overline{\operatorname{Var}} [\hat{w}_1^{(1)\top} X_1^{(1)}, \dots, \hat{w}_2^{(T)\top} X_2^{(T)}]$ be the empirical covariance of the estimated latent variables, defined in Eq. (14). Note that $\hat{\Omega} \neq \bar{\Sigma}^{-1}$ since $\hat{\Omega}$ is constrained to be sparse. Based on these estimates, we want to identify the non-zero partial cross-correlations in Ω_{12} , that is to identify the epochs of association between the two time series.

Formal inference methods for Ω based on its LaDynS estimate (Eq. (14)) are not available, but because LaDynS reduces to graphical LASSO (gLASSO) when the weights $w_k^{(t)}$ in Eq. (15) are fixed, we co-opt gLASSO inference methods. Specifically, Jankova et al. (2015) suggested de-sparsifying the gLASSO estimate $\hat{\Omega}$ according to

$$(17) \quad \tilde{\Omega} = 2\hat{\Omega} - \hat{\Omega}(\bar{\Sigma} + \lambda_{\text{diag}} I_T)\hat{\Omega},$$

and proved that, under mild assumptions and as $n \rightarrow \infty$, each entry of $\tilde{\Omega}$ satisfies the Central Limit Theorem with center the true precision Ω :

$$(18) \quad \forall(t, s), \quad \frac{(\tilde{\Omega}_{12}^{(t,s)} - \Omega_{12}^{(t,s)})}{\sqrt{\operatorname{Var}[\tilde{\Omega}_{12}^{(t,s)}]}} \xrightarrow{d} N(0, 1).$$

We applied this result to the de-sparsified LaDynS estimate of Ω , even though we do not quite have a gLASSO setup, and we verified by simulation that its elements are indeed approximately normal in Section 3.3. Jankova et al. (2015) also proposed an estimator of $\operatorname{Var}[\tilde{\Omega}_{12}^{(t,s)}]$, but it is likely to be downward biased in our framework since estimating the canonical weights $w_k^{(t)}$ induces extra randomness. Instead, we use the bootstrap estimate $\widehat{\operatorname{Var}}[\tilde{\Omega}_{12}^{(t,s)}]$ described at the end of this section, and rely on Eq. (18) to obtain p-values:

$$(19) \quad p^{(t,s)} = 2 - 2\Phi \left(|\tilde{\Omega}_{12}^{(t,s)}| / \sqrt{\widehat{\operatorname{Var}}[\tilde{\Omega}_{12}^{(t,s)}]} \right)$$

to test $H_0^{(t,s)} : \Omega_{12}^{(t,s)} = 0$, for each $(t, s) \in [T]^2$ within d_{cross} of the diagonal of Ω_{12} .

Permutation bootstrap estimate of $\operatorname{Var}[\tilde{\Omega}_{12}^{(t,s)}]$: A permutation bootstrap sample $\{X_{1[n]}^*, X_{2[n]}^*\}_{n=1, \dots, N}$ is generated by sampling a random permutation of N trials independently from each of $\{X_{1[n]}\}_{n=1, \dots, N}$ and $\{X_{2[n]}\}_{n=1, \dots, N}$. The resulting sample contains no correlated activity. Hence, applying LaDynS to the bootstrap sample yields estimates of canonical precision matrix $\hat{\Omega}^*$, canonical weights $\hat{w}_k^*(t)$ s, empirical covariance of the estimated latent variables $\bar{\Sigma}^* = \overline{\operatorname{Var}} (\hat{w}_1^{*(1)\top} X_1^{*(1)}, \dots, \hat{w}_2^{*(T)\top} X_2^{*(T)})$, and de-sparsified precision matrix estimate $\tilde{\Omega}^*$

(Eq. (17)) under the global null hypothesis of no correlated activity. Repeating the bootstrap simulation B times produces B bootstrap values $\hat{\Omega}^b$, $\hat{w}_k^{b(t)}$, $\bar{\Sigma}^b$, and $\hat{\Omega}^b$, $b = 1, \dots, B$. We estimate $\text{Var}[\tilde{\Omega}_{12}^{(t,s)}]$ with $\widehat{\text{Var}}[\tilde{\Omega}_{12}^{(t,s)}]$, the sample standard error of $\{\tilde{\Omega}_{12}^{b,(t,s)}\}_{b=1,2,\dots,B}$. Notice that $\widehat{\text{Var}}[\tilde{\Omega}_{12}^{(t,s)}]$ is obtained under the global null hypothesis – i.e. under $H_0^{(t,s)} : \Omega_{12}^{(t,s)} = 0$ simultaneously for all (t, s) – because it is not trivial to simulate bootstrap data that satisfy a specific $H_0^{(t,s)}$ without assuming that all other elements of Ω_{12} are also null. We garnered from simulations that $\widehat{\text{Var}}[\tilde{\Omega}_{12}^{(t,s)}]$ is thus likely to slightly underestimate $\text{Var}[\tilde{\Omega}_{12}^{(t,s)}]$, which makes for slightly sensitive p-values.

Control of false discoveries: Because we perform tests for many entries of Ω_{12} , we cap the false discovery rate

$$(20) \quad \text{FDR} = \mathbb{E}[\text{FDP}], \text{ where } \text{FDP} = \frac{\#\{\text{falsely discovered entries}\}}{\#\{\text{discovered entries}\} \vee 1}$$

below a pre-specified level α_{BH} using the procedure of [Benjamini and Hochberg \(1995\)](#) (BH). To proceed, let $p^{[1]} \leq \dots \leq p^{[n_{\text{roi}}]}$ denote the ordered permutation bootstrap p-values $p^{(t,s)}$ that correspond to n_{roi} cross-precision elements in the region of interest. Then, we find the maximum k_{BH} satisfying $p^{[k_{\text{BH}}]} \leq \frac{k_{\text{BH}}}{n_{\text{roi}}} \alpha_{\text{BH}}$ and reject $H_0^{(t,s)}$ with $p^{(t,s)}$ smaller than $\frac{k_{\text{BH}}}{n_{\text{roi}}} \alpha_{\text{BH}}$. The FDR guarantee is established by [Benjamini and Hochberg \(1995\)](#) as long as the $p^{(t,s)}$'s are independent and valid p-values.

Cluster-wise inference by excursion test: As a further safeguard against falsely detecting correlated activity between brain areas, we obtain p-values for each identified connectivity epoch using the excursion test of [Ventura, Cai and Kass \(2005\)](#), as follows. For each cluster k identified by the BH procedure, we calculate the test statistic:

$$(21) \quad T_k := -2 \sum_{(t,s) \in \text{cluster } k} \log p^{(t,s)},$$

which is reminiscent of Fisher's method for testing the global significance of multiple hypotheses ([Fisher, 1925](#)). We calculate the corresponding p-value as $\int_{T_k}^{\infty} f_{T_{\text{max}}}(t) dt$, since large values of T_k provide evidence against cross-area connectivity in cluster k , where $f_{T_{\text{max}}}$ is the null distribution of $T_{\text{max}} := \max_j T_j$ under the global null hypothesis of no connectivity anywhere. We use $f_{T_{\text{max}}}$ rather than the respective null distributions of each T_k to control the family-wise type I error rather than the type I error for each cluster. We approximate $f_{T_{\text{max}}}$ by the previous permutation bootstrap: for each permuted dataset $b = 1, \dots, B$, we estimate the cross-precision matrix and corresponding p-values, identify all clusters of p-values below $\frac{k_{\text{BH}}}{n_{\text{roi}}} \alpha_{\text{BH}}$, calculate the corresponding test statistics in Eq. (21), and let T_{max}^b be their maximum. The B values T_{max}^b are samples from $f_{T_{\text{max}}}$, which we use to approximate the p-value for cluster k by the sampling proportion:

$$\frac{1}{B} \sum_{b=1}^B \mathbb{I}(T_{\text{max}}^b \geq T_k).$$

2.5. Locally Stationary State-space Model and Local Granger Causality. Our model in Eqs. (7) and (8) can be formulated as a state-space model by rewriting the joint multivariate

Gaussian model for the latent vectors in Eq. (8) as the set of all conditional distributions

$$(22) \quad \begin{aligned} Z_1^{(t)} &= \sum_{s=1}^{d_{\text{auto}}} \alpha_{11,s}^{(t)} Z_1^{(t-s)} + \sum_{s=1}^{d_{\text{cross}}} \alpha_{12,s}^{(t)} Z_2^{(t-s)} + \eta_1^{(t)}, \\ Z_2^{(t)} &= \sum_{s=1}^{d_{\text{auto}}} \alpha_{22,s}^{(t)} Z_2^{(t-s)} + \sum_{s=1}^{d_{\text{cross}}} \alpha_{21,s}^{(t)} Z_1^{(t-s)} + \eta_2^{(t)}, \end{aligned}$$

where d_{auto} and d_{cross} are the maximal time delays in within-region and cross-region connection, respectively, as defined in Section 2.3, $\eta_k^{(t)}$, $k = 1, 2$, are independent $N(0, \phi_k^{(t)})$ noise random variables, and the $\alpha_{kl,s}^{(t)}$'s are vector auto-regressive coefficient parameters for the auto-correlation within region if $k = l$, $k = 1, 2$, and the cross-correlation between regions if $k \neq l$ with time lag s .

This state-space formulation is convenient to impose local stationarity on the latent time series, since the functional connectivity within and between brain regions relatively changes slowly over time, and to calculate the Granger causality between regions. We achieve the former by fitting stationary state-space models in moving windows of time. For the latter, Z_2 is said to Granger-cause Z_1 at time t if some $\alpha_{12,s}^{(t)}$ are non-zero (Ombao and Pinto, 2022) (and conversely if some $\alpha_{21,s}^{(t)}$ are non-zero). The coefficient of partial determination (partial R^2) between $(Z_2^{(t-d_{\text{cross}})}, \dots, Z_2^{(t-1)})$ and $Z_1^{(t)}$, conditional on $Z_1^{(t-d_{\text{auto}})}, \dots, Z_1^{(t-1)}$, calculated as

$$(23) \quad R_{2 \rightarrow 1}^2(t) = 1 - \frac{\text{Var}[\text{residual of Regression 1}]}{\text{Var}[\text{residual of Regression 2}]},$$

where

$$(24) \quad \begin{aligned} \text{Regression 1 : } Z_1^{(t)} &\sim Z_1^{(t-d_{\text{auto}})} + \dots + Z_1^{(t-1)} + Z_2^{(t-d_{\text{cross}})} + \dots + Z_2^{(t-1)} \\ \text{Regression 2 : } Z_1^{(t)} &\sim Z_1^{(t-d_{\text{auto}})} + \dots + Z_1^{(t-1)} \end{aligned}$$

may therefore be considered a test statistic for local Granger causality at time t . To allow a physiologically meaningful minimum connection time τ_1 from brain regions 2 to 1, we can also replace the second regression by

$$\begin{aligned} \text{Regression 2 : } Z_1^{(t)} &\sim Z_1^{(t-d_{\text{auto}})} + \dots + Z_1^{(t-1)} + Z_2^{(t-\tau_1+1)} + \dots + Z_2^{(t-1)} \\ &\quad + \mathbf{1}\{\tau_2 < d_{\text{cross}}\} \left(Z_2^{(t-d_{\text{cross}})} + \dots + Z_2^{(t-\tau_2-1)} \right), \end{aligned}$$

where $\tau_2 = d_{\text{cross}}$, unless there is reason to consider a shorter connection epoch. A plug-in estimator of $R_{2 \rightarrow 1}^2(t)$ is easily obtained from the estimated covariance matrix of

$$(25) \quad \left(Z_1^{(t)}, \dots, Z_1^{(t-d_{\text{auto}})}, Z_2^{(t-1)}, \dots, Z_2^{(t-d_{\text{cross}})} \right)$$

without actually running the regressions (Anderson-Sprecher, 1994).

Autocorrelations in the latent time series can inflate R^2 values. We therefore test the statistical significance of $R_{2 \rightarrow 1}^2(t)$ (or $R_{1 \rightarrow 2}^2(t)$) by comparing its observed value to its null distribution, obtained by repeatedly permuting the trials in one region and calculating $R_{2 \rightarrow 1}^2(t)$ in the permuted data. We used 2000 permutations in Section 4. The permuted data satisfy the null hypothesis of no cross-region connection and exhibit the same autocorrelation structure as the original latent time series.

3. LaDynS performance on simulated data. We have introduced LaDynS to estimate the dynamic connectivity between two or more multivariate time series, and we proposed inference procedures to identify when connectivity is statistically significant. We apply LaDynS to experimental data in Section 4, but first we examine its performance on simulated data that have properties similar to the experimental data. We simulate these data from the shared oscillatory driver model described in Section 3.1, which is unrelated to the LaDynS model. Appendix C.2 contains additional results based on simulated data that are consistent with the LaDynS model in Eqs. (7) and (8). The reproducible code scripts for the simulations and experimental data analyses are provided at github.com/HeejongBong/ladyns.

3.1. Simulation from a shared oscillatory driver model with time delay. We used a probabilistic model of the inter-areal coherence in local field potentials to generate LFP time series with a dynamic lead-lag relationship between two brain areas. The shared oscillatory driver model with time delay in [Ombao and Pinto \(2022\)](#) assumes that the coherence between two univariate LFP time series L_1 and L_2 is driven by a univariate latent oscillation L_0 at frequency f_0 :

$$(26) \quad L_k^{(t)} = \beta_k \cdot L_0^{(t-\tau_k)} + \eta_k^{(t)}, \quad k = 1, 2,$$

where $\eta_k^{(t)}$ is regional baseline noise, and τ_k is the lead-lag from L_0 to L_k . This model generalizes the Synaptic-Source-Mixing (SSM) model of [Schneider et al. \(2021\)](#), which was shown to be capable of modeling the dynamic cross-regional coherence observed in experimental LFP data between frontal and parietal cortices, as well as between LGN and the visual cortex.

For our simulation, we extended Eq. (26) to generate two sets of multi-dimensional LFP time series L_k of dimension d_k , $k = 1, 2$, and we used three latent oscillations $L_{0,j}$, $j = 1, 2, 3$, instead of one, to allow non-stationary lead-lag relationships between the two brain areas. The resulting model was a special case of the Latent Dynamic Factor Analysis model in [Bong et al. \(2020\)](#):

$$(27) \quad L_k^{(t)} = \sum_{j=1}^3 \beta_{kj} \cdot L_{0,j}^{(t-\tau_{kj})} + \eta_k^{(t)}, \quad k = 1, 2,$$

where the factor loadings $\beta_{kj} \in \mathbb{R}^{d_k}$ were vectors of dimension d_k ; we took $d_k = 25$. We virtually arranged the 25 components of $L_1^{(t)}$ and $L_2^{(t)}$ on 5×5 regular two-dimensional arrays so we could create simulated data exhibiting spatial correlations similar to those in the experimental data in Section 4. To do that we let $\eta_k^{(t)}$ be pink noise, as in [Schneider et al. \(2021\)](#), which is a mixture of oscillations at different frequencies f with power proportional to $f^{-\alpha}$ – we took $\alpha = 1.4$ – and we added the spatial correlations $\text{Cov}[\eta_{ki}^{(t)}, \eta_{kj}^{(t)}] = \exp(-\frac{\text{dist}^2(i,j)}{2\sigma_{\text{spatial}}^2})$, where $\text{dist}(i,j)$ was the distance between electrodes i and j on one array, with σ_{spatial} set at 0.8. Next, we let the factor loadings β_{kj} be $\beta_{kji} = \gamma \cdot \exp(-\frac{\text{dist}^2(i,p_{kj})}{2\sigma_{\text{spatial}}^2})$, $i = 1, \dots, d_k$, where p_{kj} was a randomly chosen location on an array and γ took values in $\{0.055, 0.063, 0.071, 0.077, 0.084, 0.089\}$. This set spanned $\{0.5, 0.66, 0.84, 1.0, 1.16, 1.34\}$ times the observed signal-to-noise ratio (SNR) in the experimental data in Section 4. Finally, the three latent oscillations $L_{0,j}$ were set at 14 Hz and designed to induce three epochs of lead-lag relationships between L_1 and L_2 around experimental times 80, 200 and 400 ms; L_1 lead L_2 by 30 ms during the first epoch, and L_1 lagged L_2 by 30 ms during the other two, as depicted in Figure 5a.

One simulated dataset consisted of $N = 1000$ trials of 500 ms long time series $\{L_1^{(t)} \in \mathbb{R}^{d_1}, L_2^{(t)} \in \mathbb{R}^{d_2}\}$ generated from Eq. (27) at sampling frequency 1000 Hz. We filtered the simulated LFP recordings using the complex Morlet wavelet at frequency $f_0 = 18$ Hz, and bandwidth 50 ms, the same as applied to the data in Section 4, and collected the beta oscillation amplitude envelopes as the absolute values of the filtered signals. The complex Morlet wavelet is a complex sinusoidal with a Gaussian envelope (Gabor, 1946), where the bandwidth refers to the Gaussian standard deviation. (The filtered amplitude at a given time t is essentially the amplitude that would be obtained using a harmonic regression with cosine and sine damped by the Gaussian kernel centered at t ; the wavelet formulation is computationally different and more efficient.) After downsampling the power envelopes to 100 Hz, we applied LaDynS to the resulting data X_1 and X_2 with $T = 50$ time points.

3.2. LaDynS estimation details. Because the simulated amplitude time series were very smooth, much like the experimental data, we added the regularizer λ_{diag} to the diagonal entries of the estimated correlation matrix $\hat{\Sigma}$ so it could be inverted. Our calibration strategy for λ_{diag} was as follows. Let $X_{k,i}^{(t)}$ be an observed time series and $S_{k,i} \in \mathbb{R}^{T \times T}$ be its auto-correlation matrix, $k \in \{1, 2\}$, $i \in \{1, \dots, d_k\}$. Band-pass filtering the LFP data induced auto-correlations in $X_{k,i}^{(t)}$, which we should observe in $S_{k,i}^{-1}$, unless $S_{k,i}^{-1}$ is degenerate. We thus took λ_{diag} to be such that $(S_{k,i} + \lambda_{\text{diag}} I_T)^{-1}$ displayed the expected auto-correlation. Practically, we chose λ_{diag} automatically to minimize the ℓ_2 distance between the off-diagonal entries of $(S_{k,i} + \lambda_{\text{diag}} I_T)^{-1}$ and the band-pass filter kernel-induced auto-correlation, after a scale adjustment, summed over k and i . Penalizing the diagonal introduced inevitable bias to the sparsified and desparsified LaDynS' precision estimates, $\hat{\Omega}$ and $\tilde{\Omega}$.

The other hyperparameters were set to $d_{\text{auto}} = d_{\text{cross}} = 10$, $\lambda_{\text{auto}} = 0$ and λ_{cross} , the penalty on the cross-correlation elements, was determined as per Section 2.3.1.

3.3. Results. The true cross-precision matrix Ω_{12} of data simulated from the model in Section 3.1 is unknown, so we estimate Ω_{12} by simulation. Given a simulated dataset, for each trial $n = 1, \dots, N$ and time $t = 1, \dots, T$, we use Eq. (12) to recover the true latent factors $(Z_{1,[n]}^{(t)}, Z_{2,[n]}^{(t)})$ from the simulated data $(X_{1,[n]}^{(t)}, X_{2,[n]}^{(t)})$ and known factor loadings $(\beta_1^{(t)}, \beta_2^{(t)})$. We then obtain the empirical covariance matrix of the true latent factors: $\Sigma^o := \frac{1}{N} \sum Z_{[n]} Z_{[n]}^\top$, where $Z_{[n]} = (Z_1^{(1)}, \dots, Z_2^{(T)})$, and in turn calculate the regularized precision matrix $\Omega^o := (\Sigma^o + \lambda_{\text{diag}} I)^{-1}$. We estimate the true precision matrix using the average of 200 repeats of Ω^o . Figure 5a shows the cross-regional component Ω_{12}^o of this estimate, where we see lead-lag relationships between simulated X_1 and X_2 around 80, 200, and 400 ms, as specified in Section 3.1.

Figure 5c displays the LaDynS cross precision estimate $\hat{\Omega}_{12}$ fitted to one dataset simulated under the connectivity scenario depicted in Fig. 5a, with connection strength $\gamma = 0.077$. Figure 5d shows the permutation bootstrap p-values in Eq. (19) (with permutation bootstrap simulation size $B = 200$) for the entries of the desparsified cross-precision estimate $\tilde{\Omega}_{12}$. Small p-values concentrate near the locations of true non-zero cross-precision entries and are otherwise scattered randomly. We then identified the significant connections by first applying the BH procedure with target FDR 5% and next by applying the excursion test to all discovered clusters at significance level 5% (Section 2.4). The significant clusters ($p < 0.005$) are plotted in Fig. 5e. They match approximately the true clusters in Figure 5a, although they exhibit random variability, as we should expect. To average this random variability out, we estimated $\tilde{\Omega}_{12}$ for each of 60 simulated datasets, and plotted their average in Figure 5b. The average LaDynS estimate is a close match to the true cross-precision matrix in Fig. 5a.

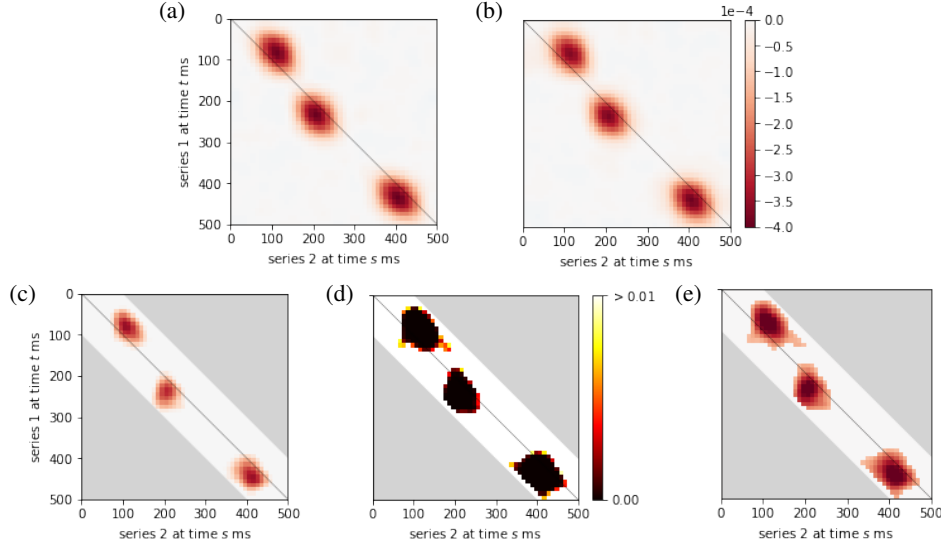


Fig 5: Output and inference of LaDynS applied to one simulated dataset from the shared oscillatory driver model. (a) True cross-precision matrix Ω_{12} , for the connectivity scenario described in Section 3.1 with $\gamma = 0.077$. (b) Average over 60 simulation datasets of LaDynS de-sparsified precision estimates $\tilde{\Omega}_{12}$. There is a good match to the true Ω_{12} in (a). (c) Cross-precision estimate $\hat{\Omega}_{12}$ for one simulated dataset. It matches (a) up to random error. (d) Permutation bootstrap p-values for the de-sparsified estimate $\tilde{\Omega}_{12}$. (e) Discovered non-zero cross-precision estimates by the BH procedure at nominal FDR 5%. The cluster-wise p-values of the three discovered clusters by the excursion test were all smaller than 0.5%. All the panels but (d) share the same color bar in (b).

Remark. We note that LaDynS is capable of estimating amplitude lead-lag relationships between two high-dimensional oscillatory time-series even if there is no coherence or phase locking between them, as reported in Appendix C.1. We demonstrated this using simulated data from the model in Section 3.1, modified so it would induce amplitude lead-lag relationships without inducing phase correlations between the simulated pair of time-series. This shows that LaDynS estimates lead-lag relationships based on correlations between the amplitudes of signals rather than from other sources of correlations, which is a defining feature of the method.

False cluster discovery rate control. We consider another measure of performance for LaDynS: cluster discovery rate control. Because the true canonical correlation matrix is unknown in our simulation study, the locations of non-zero entries in the cross-precision matrix Ω_{12} are also unknown. We did estimate Ω_{12} in Figure 5c, but the inherent variability of estimates makes it hard to evaluate accurately the false discovery and non-discovery rates for the non-zero entries of Ω_{12} . See Appendix C.2 for an example where Ω_{12} is known so these rates can be calculated. Instead, we focused on the false *cluster* discovery and non-discovery rates (Perone Pacifico et al., 2004) (FCDR, FCNR), which are less sensitive to Ω_{12} being approximated rather than known. We defined a cluster to be falsely discovered if it contained no true effect, and falsely non-discovered if no estimated cluster overlapped with it. We estimated these discovery rates with the corresponding proportions over 60 simulated datasets with true connectivity in Fig. 5a, for a range of connectivity intensities γ whose SNR in the beta-band spanned from zero to two times the estimated SNR in the LFP experimental data in Section 4.

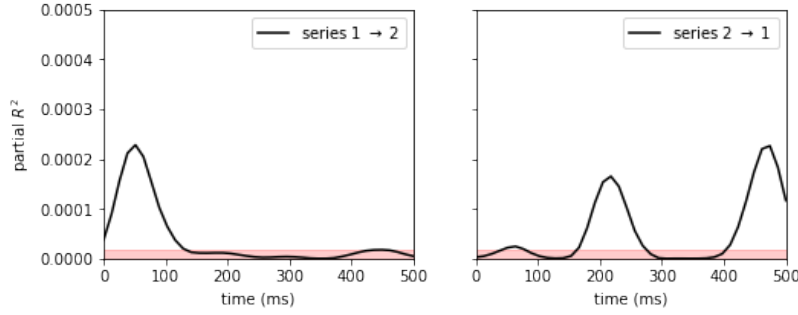


Fig 6: **Estimated partial R^2 from locally stationary state-space model.** for (left) time series $2 \rightarrow 1$ and (right) $1 \rightarrow 2$. The pink shaded areas are the 95th percentiles of null partial R^2 under independence between the two time series.

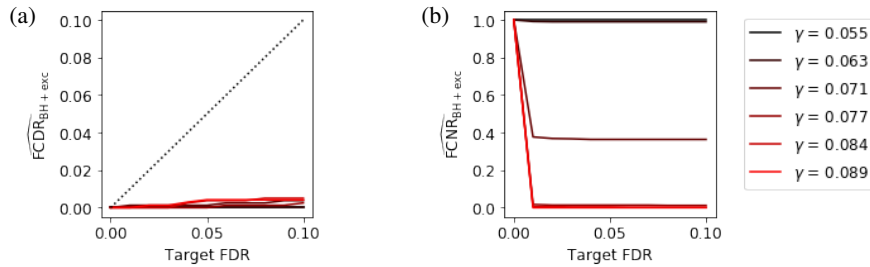


Fig 7: **Performance of cluster-wise inference after excursion test.** (a) False cluster discovery rates and (b) false cluster non-discovery rate of BH at target FDR 5% followed by excursion test at significance level $\alpha \in [0, 0.10]$ to identify non-zero partial correlations, under the connectivity scenario in Fig. 5a, for the simulated range of connectivity intensities.

In Fig. 7, the false cluster discovery/non-discovery proportions are plotted against nominal FDR values between 0 and 10%. The estimated FCDRs (Fig. 7a) were small throughout the tested range of nominal FDR values and connectivity intensities. The estimated FCNRs (Fig. 7b) were also low when true lead-lag relationships existed ($\gamma > 0$).

Checking the assumptions in Eqs. (18) and (19). Finally, we checked the assumptions of our inference method. Specifically, we assumed that the desparsified precision entries $\tilde{\Omega}_{12}^{(t,s)}$ were normally distributed (Eq. (18)) and that the permutation bootstrap estimate of variance $\widehat{\text{Var}}[\tilde{\Omega}_{12}^{(t,s)}]$ was a good approximation to $\text{Var}[\tilde{\Omega}_{12}^{(t,s)}]$ in Eq. (19) under the null hypothesis $H_0^{(t,s)} : \Omega_{12}^{(t,s)} = 0$. We investigated the validity of the Normal assumption in Eq. (18) by comparing the empirical distribution of $R = 60$ repeat estimates $\tilde{\Omega}_{12}^{(t,s)} / \sqrt{\widehat{\text{Var}}[\tilde{\Omega}_{12}^{(t,s)}]}$ to the standard normal distribution. Fig. 8 shows QQ-plots for each of three randomly chosen time pairs (t, s) that satisfy the null hypothesis $\Omega_{12}^{(t,s)} = 0$. The good agreement between empirical and theoretical quantiles suggests that the standard Gaussian null distribution in Eq. (18) is appropriate. We further checked the validity of the permutation bootstrap variance estimate $\widehat{\text{Var}}[\tilde{\Omega}_{12}^{(t,s)}]$, shown in Fig. 9a, by comparing it to the empirical variance of the $R = 60$ estimates $\tilde{\Omega}_{12}^{(t,s)}$, shown in Fig. 9b. To facilitate the comparison, Fig. 9c shows the Q-Q plot of the ratios of the permutation bootstrap estimates over the empirical estimates for all (t, s) that have $\Omega_{12}^{(t,s)} = 0$, with $F(B - 1, R - 1)$ being the reference distribution. The good agreement

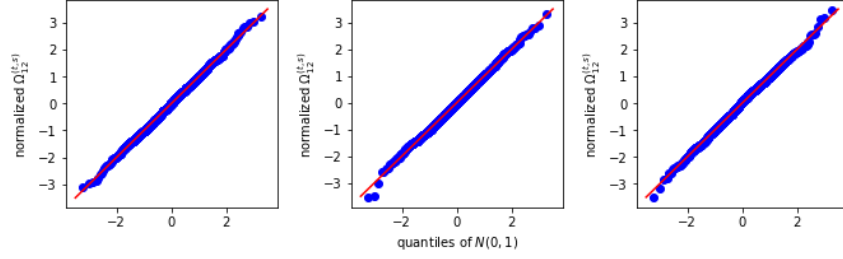


Fig 8: **Null distributions of three representative entries of $\tilde{\Omega}_{12}^{(t,s)} / \sqrt{\widehat{\text{Var}}[\tilde{\Omega}_{12}^{(t,s)}]}$.** The null distributions are obtained from $R = 60$ simulated datasets (Section 3.1) and compared to the standard Gaussian distribution via QQ-plots. There is a good agreement, which suggests that Eq. (19) is not invalidated.

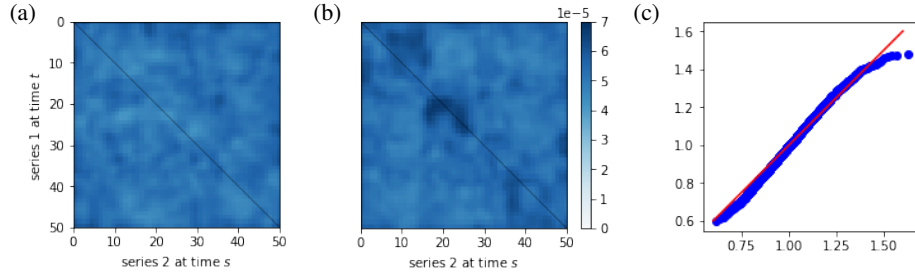


Fig 9: **Standard deviations of desparsified precision elements.** Variance obtained (a) from permutation bootstrapped samples and (b) from samples from the ground-truth generative multiset pCCA model. (c) F-statistics of ratios between the two variances for null entries of Ω_{12} , showing good agreement.

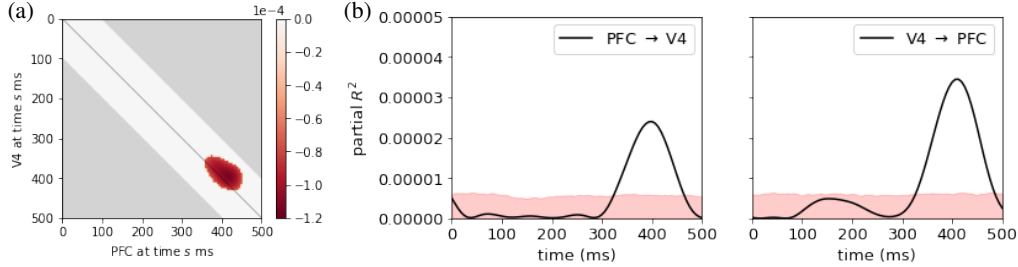


Fig 10: **Experimental data analysis.** (a) **LaDynS inference.** Discovered region of cross-precision using BH at nominal FDR 5% and the excursion test ($p < 0.0005$). The light gray area shows the region of time considered (one area leading the other by at most 100 ms). The red blob suggests that activity in V4 preceded that in PFC around 400 ms in the delay period. (b) **Estimated partial R^2 from locally stationary state-space model** for (left) $V4 \rightarrow PFC$ and (right) $PFC \rightarrow V4$. The pink shaded areas indicate the range of values that fall below the 95th percentile under the null hypothesis of independence between V4 and PFC.

between empirical and theoretical quantiles suggests that the bootstrap estimate of $\text{Var}[\Omega_{12}^{(t,s)}]$ is reliable.

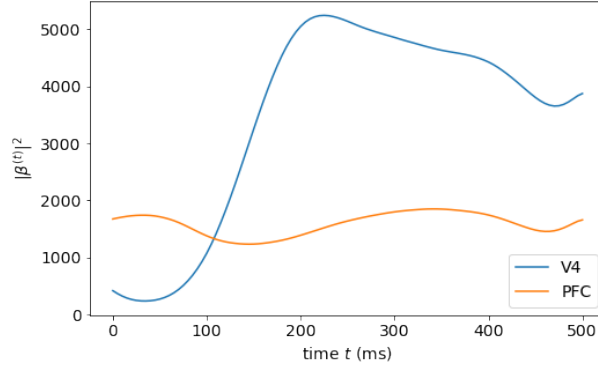


Fig 11: **Estimated beta powers of electrophysiological activity driven by latent factors in V4 and PFC as functions of time.** The ℓ_2 norm of the factor loading vector $\beta_k^{(t)}$ represents the summed beta power in the data $X_k^{(t)}$ attributable to the latent time series at time t ; see Eq. (7).

4. Experimental Data Analysis. We applied LaDynS to local field potentials (LFPs), collected in the experiment described in [Khanna, Scott and Smith \(2020\)](#), from two Utah arrays implanted in a Macaque monkey’s prefrontal cortex (PFC) and V4 during a memory-guided saccade task. Each trial of the task started with a monkey fixating its eyes toward the center of the screen. A visual cue was given for 50 ms to indicate a target location, which was randomly chosen from 40 locations that tiled the display screen. The cue was turned off and the monkey had to remember the target location while maintaining eye fixation for a delay period of 500 ms. After the delay period, the monkey reoriented its eyes toward the remembered position, and reward was given on successful trials. As in [Khanna, Scott and Smith \(2020\)](#), we analyzed the time series during the delay period, based on 3000 successful trials. Time $t = 0$ corresponds to the start of that period. The data are available in [Snyder, Johnston and Smith \(2022\)](#). Because beta oscillations are often associated with communication across brain areas ([Klein et al., 2020](#); [Miller, Lundqvist and Bastos, 2018](#)), we first filtered LFP recordings at a beta oscillation frequency 18 Hz and obtained the beta oscillation power envelopes as described in Section 3.1. We chose 18 Hz because it was the frequency having the largest power within the range 12-40 Hz (see Fig. D.1). After downsampling the power envelopes to 200 Hz, we applied LaDynS with the regularizer λ_{diag} on the diagonal of Σ , as in Section 3.2, because the filtered data were very smooth.

Figure 10a shows the only epoch of significant contiguous region of the precision matrix identified by our method (red blob, FDR at 5%, $p < .0005$ by the excursion test in Section 2.4). This result provides strong evidence that the 18 Hz beta amplitudes in PFC and V4 were correlated (after conditioning on beta amplitudes at all other times and lags) around 400 milliseconds after the start of the delay period.

To better understand this relationship, we used the estimated latent time series to compute partial R^2 values under an assumption of locally stationarity, applying the model in Eq. (22), Section 2.5. The frequency 18 Hz corresponds to a period of 55 ms and it is hard to detect non-stationarity at time scales finer than a few periods. We used a moving window of 100 ms to calculate partial R^2 , allowing connection delays between V4 and PFC in the $\tau_1 = 15$ to $\tau_2 = 30$ ms range. The partial R^2 from V4 to PFC and from PFC to V4 are shown in Fig. 10b. There are large excursions of R^2 above the null values in both plots, suggesting that, at around 400 ms post stimulus, the two areas are involved in a bidirectional network: the power of the activity in each area predicts the power of the oscillation in the other, following a short delay (after conditioning on the power at all other times and lags). To see that this is not due solely

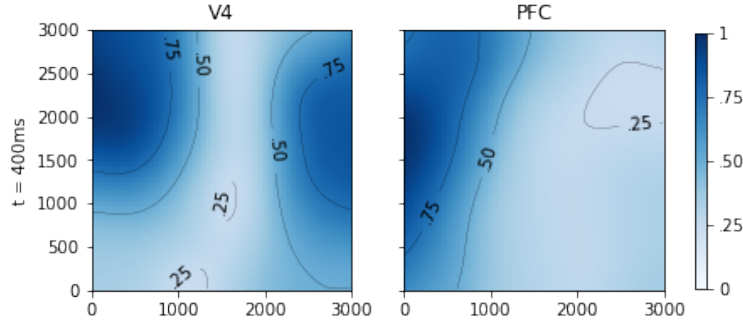


Fig 12: **Factor loadings of V4 and PFC**, spatially smoothed, normalized, and color coded over the electrode coordinates (μm) on (left) V4 and (right) PFC at late delay period (400 ms). Contours at .25, .5 and .75 of the maximal power were added.

to the activity passing through the visual stream, in Fig. 11, for each of the two latent time series, we plot the estimated total beta power as a function of time. The power in V4 increases dramatically much earlier than 400 ms, starting around 100 ms and reaching a peak just after 200 ms; it then remains substantial during the remainder of the delay period. The results in Fig. 10 can not be explained by those in Fig. 11 alone.

It is also possible to get spatial information from the normalized factor loadings across the electrode arrays, which are displayed in Fig. 12 for experimental time 400 ms. The loadings were rescaled by their maximal value across the array. (An animation over the complete timeline is available at github.com/HeejongBong/ladyns.) It is apparent that a relatively small proportion of the electrodes, residing in limited portions of the recording areas, contribute most of the beta oscillatory power identified by the bivariate time series.

5. Discussion. Motivated by the problem of describing interactions in oscillatory amplitudes of high-dimensional neural field potentials across a pair of brain regions we have provided a time-series extension of probabilistic CCA together with a novel sparse estimation methodology. According to our Equation (7), each of the two multivariate time series is driven by a single latent time series, with the cross-dependence of these two latent time series representing cross-region interaction. According to Equation (8), the latent bivariate time series is a discrete Gaussian process but its correlation matrix is unrestricted, allowing for non-stationarity. The repeated trial structure enabled us to estimate the resulting high-dimensional covariance matrix, by applying sparse estimation and inference methods. We found, and displayed in Fig. 10b, an interesting interaction between PFC and V4, involving beta power, that appeared during late delay period, with the interaction being bidirectional. The results were based on partial R^2 values, computed from the estimated covariance matrices, corresponding to lagged regressions of one latent time series on the other. The analysis in Fig. 10b is in the spirit of Granger causality, but differs from it by allowing for non-stationarity, so that we could obtain the time-varying results.

The partial R^2 values in Fig. 10b are highly statistically significant, but they are very small. We note that our diagonal regularization of the estimated latent precision matrix artificially reduced these values, so that the scale is no longer interpretable in familiar terms. The cross-correlation estimates are several orders of magnitude larger (see Fig. D.2). However, they remain smaller than .1, as are the raw correlations at 400 ms and 425 ms, respectively, across individual electrodes in V4 and PFC (not shown). This reflects the highly inhomogeneous nature of the LFP voltage recordings together with the dominance of low frequencies (unfiltered LFP spectra typically follow $1/f^k$ trends, where f is frequency and k is roughly 1.5 to 2). The large number of repeated trials allowed us to find and document the results.

In addition to making the analysis possible, the repeated trial structure suggests substantive interpretation based on trial-to-trial variability. Although investigators take pains to make the experimental setting nearly the same on each trial, the inevitable small fluctuations in the way the subject interacts with the environment, together with changes in the subject's underlying state (involving alterations in motivational drive, for example), lead to observable fluctuations in behavior and in the recorded neural activity. Although the network sources of trial-to-trial variability in the PFC and V4 data are unknown, they produce the kind of correlated activity revealed in Fig. 10b. To interpret it, we acknowledge there could be some task-irrelevant, trial-varying pulses of inputs that drive beta power in V4 and PFC, having just the right differential time lags to produce the correlated activity picked up by the partial R^2 values. Could such task-irrelevant pulses of activity change across time, within repetitions of the task, in such a way as to produce, the peaks in Fig. 10b? It is possible, but it would be surprising, especially when we consider contemporary ideas about beta oscillations during working memory tasks (Miller, Lundqvist and Bastos, 2018) along with the well-identified distinction between early and late visual processing that, presumably, corresponds to a distinction between feedforward and recurrent (bidirectional) flow of information (Chen et al., 2022; Del Cul, Baillet and Dehaene, 2007; Supér, Spekreijse and Lamme, 2001; Yang et al., 2019). The alternative we mentioned, that PFC and V4 are involved, together, in goal-directed visual processing and memory, with the two areas acting bidirectionally around 400 ms post stimulus, seems likely.

There are many ways to extend the ideas developed here. For band-pass filtered data, such as those analyzed in Section 4, phase analysis (Klein et al., 2020) could be combined with amplitude analysis based on the complex normal distribution, as in Urban et al. (2023) (which developed a latent variable model at a single time point). Multiple frequencies could be considered, along the lines of Gallagher et al. (2017), as well. In Bong et al. (2020) we have described an extension of LaDynS, where the within-region noise vectors ϵ_k were allowed to have general time series structure and the latent time series driving each brain region were multidimensional. That brief report (using data filtered at a different frequency) does not provide the details given here, nor does it include inferential procedures. A future step would be to generalize the methods here to the setting of Bong et al. (2020). A different direction for additional research would be to simplify the version of LaDynS we have used here by imposing suitable spatiotemporal structure on the latent time series. Regardless of whether such approaches are fruitful, the general framework of LaDynS could be of use whenever interest focuses on non-stationary interactions among groups of repeatedly-observed multivariate time series.

Acknowledgements. Bong, Ventura and Kass are supported in part by NIMH grant R01 MH064537. Yttri is supported by NIH grant (1R21EY029441-01) and the Whitehall Foundation. Smith is supported by NIH (R01EY022928, R01MH118929, R01EB026953, P30EY008098) and NSF (NCS 1734901) grants.

SUPPLEMENTARY MATERIAL

Supplement A: Supplement to "Cross-Population Amplitude Coupling in High-Dimensional Oscillatory Neural Time Series"

(doi: [COMPLETED BY THE TYPESETTER](#); .pdf). A PDF manuscript providing supplemental descriptions of proofs, algorithms, and extensive details regarding arguments conveyed in the main text.

Supplement B: LaDynS Code Package with Reproducible Examples to "Cross-Population Amplitude Coupling in High-Dimensional Oscillatory Neural Time Series"

(doi: [COMPLETED BY THE TYPESETTER](#); .zip). LaDynS Python package with tutorials based on the reproducible scripts generating the results given in the main text. The latest version will be updated at github.com/HeejongBong/ladyns.

REFERENCES

- ANDERSON-SPRECHER, R. (1994). Model Comparisons and R2. *The American Statistician* **48** 113–117.
- BACH, F. R. and JORDAN, M. I. (2005). A probabilistic interpretation of canonical correlation analysis Technical Report No. 688, Department of Statistics, University of California, Berkeley, Berkeley, CA.
- BENJAMINI, Y. and HOCHBERG, Y. (1995). Controlling the false discovery rate: a practical and powerful approach to multiple testing. *Journal of the Royal statistical society: series B (Methodological)* **57** 289–300.
- BONG, H., LIU, Z., REN, Z., SMITH, M. A., VENTURA, V. and KASS, R. E. (2020). Latent Dynamic Factor Analysis of High-Dimensional Neural Recordings. *Advances in Neural Information Processing Systems* **33**.
- BUZSÁKI, G., ANASTASSIOU, C. A. and KOCH, C. (2012). The origin of extracellular fields and currents—EEG, ECoG, LFP and spikes. *Nature reviews neuroscience* **13** 407–420.
- CHEN, Y., DOUGLAS, H., MEDINA, B. J., OLARINRE, M., SIEGLE, J. H. and KASS, R. E. (2022). Population Burst Propagation Across Interacting Areas of the Brain. *Journal of Neurophysiology*.
- DEL CUL, A., BAILLET, S. and DEHAENE, S. (2007). Brain dynamics underlying the nonlinear threshold for access to consciousness. *PLoS biology* **5** e260.
- FISHER, R. A. (1925). *Statistical Methods for Research Workers* **3**. Oliver and Boyd.
- FRIEDMAN, J., HASTIE, T. and TIBSHIRANI, R. (2008). Sparse inverse covariance estimation with the graphical lasso. *Biostatistics* **9** 432–441.
- FRIES, P., REYNOLDS, J. H., RORIE, A. E. and DESIMONE, R. (2001). Modulation of oscillatory neuronal synchronization by selective visual attention. *Science* **291** 1560–1563.
- GABOR, D. (1946). Theory of communication. Part 1: The analysis of information. *Journal of the Institution of Electrical Engineers-part III: radio and communication engineering* **93** 429–441.
- GALLAGHER, N., ULRICH, K. R., TALBOT, A., DZIRASA, K., CARIN, L. and CARLSON, D. E. (2017). Cross-spectral factor analysis. In *Advances in neural information processing systems* 6842–6852.
- GOKCEN, E., JASPER, A. I., SEMEDO, J. D., ZANDVAKILI, A., KOHN, A., MACHENS, C. K. and YU, B. M. (2021). Disentangling the flow of signals between populations of neurons. *bioRxiv*.
- HOTELLING, H. (1992). Relations between two sets of variates. In *Breakthroughs in statistics* 162–190. Springer.
- JANKOVA, J., VAN DE GEER, S. et al. (2015). Confidence intervals for high-dimensional inverse covariance estimation. *Electronic Journal of Statistics* **9** 1205–1229.
- JUN, J. J., STEINMETZ, N. A., SIEGLE, J. H., DENMAN, D. J., BAUZA, M., BARBARITS, B., LEE, A. K., ANASTASSIOU, C. A., ANDREI, A., AYDIN, Ç. et al. (2017). Fully integrated silicon probes for high-density recording of neural activity. *Nature* **551** 232–236.
- KETTENRING, J. R. (1971). Canonical analysis of several sets of variables. *Biometrika* **58** 433–451.
- KHANNA, S. B., SCOTT, J. A. and SMITH, M. A. (2020). Dynamic shifts of visual and saccadic signals in prefrontal cortical regions 8Ar and FEF. *Journal of Neurophysiology*. In press.
- KLEIN, N., ORELLANA, J., BRINCAT, S. L., MILLER, E. K., KASS, R. E. et al. (2020). Torus graphs for multivariate phase coupling analysis. *Annals of Applied Statistics* **14** 635–660.
- LAKSHMANAN, K. C., SADTLER, P. T., TYLER-KABARA, E. C., BATISTA, A. P. and YU, B. M. (2015). Extracting low-dimensional latent structure from time series in the presence of delays. *Neural computation* **27** 1825–1856.
- LIEBE, S., HOERZER, G. M., LOGOTHETIS, N. K. and RAINER, G. (2012). Theta coupling between V4 and prefrontal cortex predicts visual short-term memory performance. *Nature neuroscience* **15** 456.
- MAZUMDER, R. and HASTIE, T. (2012). The graphical lasso: New insights and alternatives. *Electronic journal of statistics* **6** 2125.
- MILLER, E. K. and COHEN, J. D. (2001). An integrative theory of prefrontal cortex function. *Annual review of neuroscience* **24** 167–202.
- MILLER, E. K., LUNDQVIST, M. and BASTOS, A. M. (2018). Working Memory 2.0. *Neuron* **100** 463–475.
- OMBAO, H. and PINTO, M. (2022). Spectral dependence. *Econometrics and Statistics*.
- ORBAN, G. A. (2008). Higher order visual processing in macaque extrastriate cortex. *Physiological reviews* **88** 59–89.
- PERONE PACIFICO, M., GENOVESE, C., VERDINELLI, I. and WASSERMAN, L. (2004). False discovery control for random fields. *Journal of the American Statistical Association* **99** 1002–1014.
- PESARAN, B., VINCK, M., EINEVOLL, G. T., SIROTA, A., FRIES, P., SIEGEL, M., TRUCCOLO, W., SCHROEDER, C. E. and SRINIVASAN, R. (2018). Investigating large-scale brain dynamics using field potential recordings: analysis and interpretation. *Nature neuroscience* **21** 903–919.

- SARNTHEIN, J., PETSCH, H., RAPPELSBERGER, P., SHAW, G. and VON STEIN, A. (1998). Synchronization between prefrontal and posterior association cortex during human working memory. *Proceedings of the National Academy of Sciences* **95** 7092–7096.
- SCHMIDT, R., RUIZ, M. H., KILAVIK, B. E., LUNDQVIST, M., STARR, P. A. and ARON, A. R. (2019). Beta oscillations in working memory, executive control of movement and thought, and sensorimotor function. *Journal of Neuroscience* **39** 8231–8238.
- SCHNEIDER, M., BROGGINI, A. C., DANN, B., TZANOU, A., URAN, C., SHESHADRI, S., SCHERBERGER, H. and VINCK, M. (2021). A mechanism for inter-areal coherence through communication based on connectivity and oscillatory power. *Neuron* **109** 4050–4067.
- SEMEDO, J. D., GOKCEN, E., MACHENS, C. K., KOHN, A. and YU, B. M. (2020). Statistical methods for dissecting interactions between brain areas. *Current opinion in neurobiology* **65** 59–69.
- SHAO, J. (1993). Linear model selection by cross-validation. *Journal of the American statistical Association* **88** 486–494.
- SNYDER, A., JOHNSTON, R. and SMITH, M. (2022). Utah array recordings from visual cortical area V4 and prefrontal cortex with simultaneous EEG.
- STEINMETZ, N. A., KOCH, C., HARRIS, K. D. and CARANDINI, M. (2018). Challenges and opportunities for large-scale electrophysiology with Neuropixels probes. *Current opinion in neurobiology* **50** 92–100.
- SUPÈR, H., SPEKREIJSE, H. and LAMME, V. A. (2001). Two distinct modes of sensory processing observed in monkey primary visual cortex (V1). *Nature neuroscience* **4** 304–310.
- TIBSHIRANI, R. J., TAYLOR, J. et al. (2012). Degrees of freedom in lasso problems. *The Annals of Statistics* **40** 1198–1232.
- URBAN, K., BONG, H., ORELLANA, J. and KASS, R. E. (2023). Oscillating neural circuits: Phase, amplitude, and the complex normal distribution. Under review.
- VENTURA, V., CAI, C. and KASS, R. E. (2005). Statistical assessment of time-varying dependency between two neurons. *Journal of Neurophysiology* **94** 2940–2947.
- WILKS, S. S. (1932). Certain generalizations in the analysis of variance. *Biometrika* 471–494.
- YANG, Y., TARR, M. J., KASS, R. E. and AMINOFF, E. M. (2019). Exploring spatiotemporal neural dynamics of the human visual cortex. *Human brain mapping* **40** 4213–4238.
- YU, B. M., CUNNINGHAM, J. P., SANTHANAM, G., RYU, S. I., SHENOY, K. V. and SAHANI, M. (2009). Gaussian-Process Factor Analysis for Low-Dimensional Single-Trial Analysis of Neural Population Activity. *Journal of Neurophysiology* **102** 614–635. PMID: 19357332.
- ZHU, Y. and CRIBBEN, I. (2018). Sparse graphical models for functional connectivity networks: best methods and the autocorrelation issue. *Brain connectivity* **8** 139–165.
- ZOU, H., HASTIE, T., TIBSHIRANI, R. et al. (2007). On the “degrees of freedom” of the lasso. *The Annals of Statistics* **35** 2173–2192.

SUPPLEMENT TO "CROSS-POPULATION ANALYSIS OF HIGH-DIMENSIONAL NON-STATIONARY NEURAL OSCILLATIONS"

BY HEEJONG BONG¹, VALÉRIE VENTURA^{1,2,5}, ERIC YTTRI^{3,5},
MATTHEW A. SMITH^{4,5} AND ROBERT E. KASS^{1,2,5,*}

¹Department of Statistics and Data Sciences, Carnegie Mellon University, *kass@stat.cmu.edu

²Machine Learning Department, Carnegie Mellon University,

³Department of Biological Sciences, Carnegie Mellon University,

⁴Department of Biomedical Engineering, Carnegie Mellon University,

⁵Neuroscience Institute, Carnegie Mellon University,

APPENDIX A: PROOF OF THEOREMS 2.2 AND 2.3

In the model of Eqs. (7) and (8), the marginal covariance matrix S of has sub-matrices $S_{kl}^{(t,s)} = \beta_k^{(t)} \Sigma_{kl}^{(t,s)} \beta_l^{(s)\top} + \Phi_k^{(t)} \delta_{kl}^{(t,s)}$, where $\delta_{kl}^{(t,s)} = 1$ if $k = l$ and $t = s$ and 0 otherwise, for $t, s \in [T]$ and $k, l = 1, 2$. Let $u_k^{(t)} = S_{kk}^{(t,t)-\frac{1}{2}} \beta_k^{(t)}$ and $\Psi_k^{(t)} = S_{kk}^{(t,t)-\frac{1}{2}} \Phi_k^{(t)} S_{kk}^{(t,t)-\frac{1}{2}}$. We note that $u_k^{(t)\top} u_k^{(t)} = \beta_k^{(t)\top} S_{kk}^{(t,t)-1} \beta_k^{(t)} \leq 1$. Because $\beta_k^{(t)\top} S_{kk}^{(t,t)-1} \beta_k^{(t)}$ is non-identifiable, by adjusting $\Sigma_{k,l}^{(t,s)}$ and $\Phi_k^{(t)}$ for $(k, t) \neq (l, s)$, we can assume $\beta_k^{(t)\top} S_{kk}^{(t,t)-1} \beta_k^{(t)} = 1$. Then

$$\begin{aligned} u_k^{(t)\top} \Psi_{kk}^{(t)} u_k^{(t)} &= \beta_k^{(t)\top} S_{kk}^{(t,t)-1} \Phi_k^{(t)} S_{kk}^{(t,t)-1} \beta_k^{(t)} \\ &= \beta_k^{(t)\top} S_{kk}^{(t,t)-1} (S_{kk}^{(t,t)} - \beta_k^{(t)} \beta_k^{(t)\top}) S_{kk}^{(t,t)-1} \beta_k^{(t)} \\ &= \beta_k^{(t)\top} S_{kk}^{(t,t)-1} \beta_k^{(t)} - (\beta_k^{(t)\top} S_{kk}^{(t,t)-1} \beta_k^{(t)})^2 \\ &= 1 - 1^2 = 0, \end{aligned}$$

for $t \in [T]$ and $k \in \{1, 2\}$. That is, $u_k^{(t)}$ is orthogonal to $\Psi_{kk}^{(t)}$.

Denoting the block diagonal matrix consisting of $\{S_{kk}^{(t,t)} : t \in [T], k \in \{1, 2\}\}$ by V , $R = V^{-\frac{1}{2}} S V^{-\frac{1}{2}}$ consists of sub-matrices

$$R_{kl}^{(t,s)} = S_{kk}^{(t,t)-\frac{1}{2}} S_{kl}^{(t,s)} S_{ll}^{(s,s)-\frac{1}{2}} = u_k^{(t)} \Sigma_{kl}^{(t,s)} u_l^{(s)\top} + \Psi_k^{(t)} \delta_{kl}^{(t,s)}.$$

Due to the orthogonality between $u_k^{(t)}$ and $\Psi_k^{(t)}$, $\det(R) = \det(\Omega) / \prod_{k,t} \text{pdet}(\Psi_k^{(t)})$, and $Q = R^{-1}$ consists of sub-matrices

$$Q_{kl}^{(t,s)} = u_k^{(t)} \Omega_{kl}^{(t,s)} u_l^{(s)\top} + \Psi_k^{(t)+} \delta_{kl}^{(t,s)},$$

where $\Omega = \Sigma^{-1}$ is the precision matrix and $\text{pdet}(A)$ and A^+ are the pseudo-determinant and Moore-Penrose pseudo-inverse of a positive semi-definite matrix A . Notice that $\Psi_k^{(t)} = I - u_k^{(t)} u_k^{(t)\top} = \Psi_k^{(t)+}$ and hence $\text{pdet}(\Psi_k^{(t)}) = 1$. In turn, the negative log-likelihood under

the model (Eqs. (7) and (8)) given observed time-series $\{X_{1,[n]}, X_{2,[n]}\}_{n=1,\dots,N}$ is

(A.1)

$$\begin{aligned} & \text{nll}(\Sigma, \{\mu_k^{(t)}, \beta_k^{(t)}, \Phi_k^{(t)}\}_{(k,t)}; \{X_{1,[n]}, X_{2,[n]}\}_{n=1,\dots,N}) \\ &= -\log \det(\Omega) + \sum_{k,t} \log \text{pdet}(\Psi_k^{(t)}) + \sum_{k,t} \log \det(S_{kk}^{(t,t)}) \\ & \quad + \text{tr}(\Omega \bar{\Sigma}) + \sum_{k,t} \text{tr}(\Psi_k^{(t)} + S_{kk}^{(t,t)-\frac{1}{2}} \bar{S}_{kk}^{(t,t)} S_{kk}^{(t,t)-\frac{1}{2}}) \\ &= -\log \det(\Omega) + \text{tr}(\Omega \bar{\Sigma}) + \sum_{k,t} \left\{ \log \det(S_{kk}^{(t,t)}) + \text{tr}((S_{kk}^{(t,t)-1} - w_k^{(t)} w_k^{(t)\top}) \bar{S}_{kk}^{(t,t)}) \right\} \end{aligned}$$

where $\bar{\Sigma}_{kl}^{(t,s)} = w_k^{(t)\top} \bar{S}_{kl}^{(t,s)} w_l^{(s)}$, $\bar{S}_{kl}^{(t,s)} = \mathbb{E}[(X_k^{(t)} - \mu_k^{(t)})(X_l^{(s)} - \mu_l^{(s)})^\top]$ and $w_k^{(t)} = S_{kk}^{-1/2} u_k$ for $t, s \in [T]$ and $k, l \in \{1, 2\}$, and \mathbb{E} indicates the sample variance mean. Due to the first-order optimality with respect to $\mu_k^{(t)}$, $\mu_k^{(t)} = \mathbb{E}[X_k^{(t)}]$ for $k \in \{1, 2\}$ and $t \in [T]$. On the other hand, due to the first-order optimality with respect to $S_{kk}^{(t,t)-1}$, for all $k \in \{1, 2\}$ and $t \in [T]$,

$$\nabla_{S_{kk}^{(t,t)-1}} \text{nll} = S_{kk}^{(t,t)} - \bar{S}_{kk}^{(t,t)} = S_{kk}^{(t,t)} w_k^{(t)} \lambda_k^{(t)} w_k^{(t)\top} S_{kk}^{(t,t)},$$

where $\lambda_k^{(t)} \in \mathbb{R}$ is the Lagrange multiplier corresponding to $w_k^{(t)\top} S_{kk}^{(t,t)} w_k^{(t)} = 1$. Because $w_k^{(t)\top} S_{kk}^{(t,t)} w_k^{(t)} = 1$,

$$\begin{aligned} 1 - w_k^{(t)\top} \bar{S}_{kk}^{(t,t)} w_k^{(t)} &= w_k^{(t)\top} S_{kk}^{(t,t)} w_k^{(t)} - w_k^{(t)\top} \bar{S}_{kk}^{(t,t)} w_k^{(t)} \\ &= w_k^{(t)\top} S_{kk}^{(t,t)} w_k^{(t)} \lambda_k^{(t)} w_k^{(t)\top} S_{kk}^{(t,t)} w_k^{(t)} = \lambda_k^{(t)}. \end{aligned}$$

Therefore, the two terms $\log \det(S_{kk}^{(t,t)})$ and $\text{tr}((S_{kk}^{(t,t)-1} - w_k^{(t)} w_k^{(t)\top}) \bar{S}_{kk}^{(t,t)})$ are rewritten by

$$\begin{aligned} \log \det(S_{kk}^{(t,t)}) &= -\log(1 - \lambda_k^{(t)}) + \log \det(\hat{S}_{kk}^{(t,t)}), \\ \text{tr}((S_{kk}^{(t,t)-1} - w_k^{(t)} w_k^{(t)\top}) \bar{S}_{kk}^{(t,t)}) &= \text{tr}((S_{kk}^{(t,t)-1} - w_k^{(t)} w_k^{(t)\top})(S_{kk}^{(t,t)} - S_{kk}^{(t,t)} w_k^{(t)} \lambda_k^{(t)} w_k^{(t)\top} S_{kk}^{(t,t)})) \\ &= d_k - 1 \end{aligned}$$

Plugging it to Eq. (A.1), the MLE reduces to minimizing

$$\text{nll}(\Omega, w_k^{(t)}, \lambda_k^{(t)}; \{X_{1,[n]}, X_{2,[n]}\}_{n=1,\dots,N}) = -\log \det(\Omega) - \sum_{k,t} \log(1 - \lambda_k^{(t)}) + \text{tr}(\Omega \bar{\Sigma})$$

such that $\text{diag}(\Omega^{-1}) = \mathbf{1}$. Let $w_k'^{(t)} = w_k^{(t)} / \sqrt{1 - \lambda_k^{(t)}}$, $\Omega' = \text{diag}(\sqrt{1 - \lambda_k^{(t)}}) \Omega \text{diag}(\sqrt{1 - \lambda_k^{(t)}})$, and $\bar{\Sigma}' = \overline{\text{Var}}[w_1'^{(1)\top} X_1^{(1)}, \dots, w_2'^{(T)\top} X_2^{(T)}]$. Note that $\text{diag}(\bar{\Sigma}') = \mathbf{1}$. The objective is rewritten by

$$\text{nll}(\Omega', w_k'^{(t)}; \{X_{1,[n]}, X_{2,[n]}\}_{n=1,\dots,N}) = -\log \det(\Omega') + \text{tr}(\Omega' \bar{\Sigma}')$$

which is maximized when $\Omega' = \bar{\Sigma}'^{-1}$ given $w_k'^{(t)}$'s are fixed. Thus, the maximum likelihood estimation is equivalent to finding $w_k'^{(t)}$ minimizing $\log \det(\bar{\Sigma}')$ under $w_k'^{(t)\top} \bar{S}_{kk}^{(t,t)} w_k'^{(t)} = 1$ for $k \in [K]$, which is the GENVAR procedure of Kettenring (1971). This proves the desired results for the MLE with $m_k^{(t)} = 1$. The other MLEs with $m_k^{(t)} < 1$ correspond to the non-identifiable parameter sets, which have $u_k^{(t)\top} u_k^{(t)} < 1$.

Theorem 2.2 is a corollary of Theorem 2.3. To see that, let $T = 1$ so that $X_1 \equiv X_1^{(1)}$, $X_2 \equiv X_2^{(1)}$ and $\Sigma = \begin{pmatrix} 1 & \Sigma_{12}^{(1,1)} \\ \Sigma_{12}^{(1,1)\top} & 1 \end{pmatrix} = \begin{pmatrix} 1 & \sigma_{12} \\ \sigma_{12} & 1 \end{pmatrix}$. The GENVAR procedure solves

$$\operatorname{argmin}_{w_1, w_2} \det \left(\overline{\operatorname{Var}} \left[w_1^\top X_1, w_2^\top X_2 \right] \right) \equiv \operatorname{argmin}_{w_1, w_2} \det \left(\begin{pmatrix} 1 & \bar{\sigma}_{12} \\ \bar{\sigma}_{12} & 1 \end{pmatrix} \right),$$

where $\bar{\sigma}_{12} = \frac{w_1^\top \bar{\Sigma}_{12} w_2}{\sqrt{w_1^\top \bar{\Sigma}_1 w_1} \sqrt{w_2^\top \bar{\Sigma}_2 w_2}}$. This minimization problem is equivalent to the CCA problem in Eq. (1) and $\overline{\operatorname{Var}} [\hat{w}_1^\top X_1, \hat{w}_2^\top X_2] = \begin{pmatrix} 1 & \hat{\sigma}_{cc} \\ \hat{\sigma}_{cc} & 1 \end{pmatrix}$, which implies $\hat{\beta}_k = \bar{\Sigma}_{kk} \hat{w}_k m_k$ and $m_1 m_2 \hat{\sigma}_{12} = \hat{\sigma}_{cc}$ for $|m_k| \leq 1$, as in Theorem 2.2.

APPENDIX B: FITTING LADYNS

Algorithm 1 Coordinate descent algorithm to fit LaDynS**Input:**

$\{X_k : k = 1, \dots, K\}$: input data
 $\Lambda \in [0, \infty]^{KT \times KT}$: sparsity penalty matrix
 $\text{iter}_{\max} \in \mathbb{N}_+$: maximum iteration
 $\text{ths} \in \mathbb{R}_+$: threshold for convergence

Output: Ω and $w_k^{(t)}$'s which solve Eq. (14) w.r.t. Fig. 4

Initialization:

1: Initialize $w_k^{(t)}$ so that $w_k^{(t)\top} \overline{\text{Var}}[X_k^{(t)}] w_k^{(t)} = 1$ for all $t \in [T]$ and $k = 1, 2$. e.g.,

$$(B.1) \quad w_k^{(t)} \leftarrow \mathbf{1} / \sqrt{\mathbf{1}^\top \overline{\text{Var}}[X_k^{(t)}] \mathbf{1}}.$$

and let

$$(B.2) \quad \overline{\Sigma} \leftarrow \overline{\text{Var}}[w_1^{(1)\top} X_1^{(1)}, \dots, w_2^{(T)\top} X_2^{(T)}].$$

2: Initialize Σ and Ω by

$$(B.3) \quad \Sigma \leftarrow \overline{\Sigma} + \lambda_{\text{diag}} I_{2T} \text{ and } \Omega \leftarrow \Sigma^{-1}.$$

Iteration:

3: **for** iter in 1:iter_{max} **do**

4: $\Sigma_{\text{last}} \leftarrow \Sigma, \Omega_{\text{last}} \leftarrow \Omega$

5: $\Sigma, \Omega \leftarrow \text{P-gLASSO}(\Omega_{\text{init}}, \Sigma_{\text{init}}, \overline{\Sigma}, \Lambda, \text{iter}_{\max}, \text{ths})$.

6: **for** k in 1:2 and t in 1:T **do**

7: $A \leftarrow \overline{\text{Cov}}[X_k^{(t)}, (Y_l^{(s)} : (l, s) \neq (k, t))]$.

8: $b \leftarrow (\Omega_{kl}^{(t,s)} : (l, s) \neq (k, t))$

9: **if** $Ab \neq \mathbf{0}$ **then**

10: $w_k^{(t)} \leftarrow \overline{\text{Var}}(X_k^{(t)})^{-1} Ab$

11: $w_k^{(t)} \leftarrow w_k^{(t)} / \sqrt{w_k^{(t)\top} \overline{\text{Var}}[X_k^{(t)}] w_k^{(t)}}$

12: **end if**

13: **end for**

14: $\overline{\Sigma} \leftarrow \overline{\text{Var}}[w_1^{(1)\top} X_1^{(1)}, \dots, w_2^{(T)\top} X_2^{(T)}]$.

15: **if** $\max(|\Sigma - \Sigma_{\text{last}}|) < \text{ths}$ **then**

16: **break**

17: **end if**

18: **end for**

B.1. Coordinate Descent Algorithm. To update Ω , we use the P-gLASSO algorithm of Mazumder and Hastie (2012), which is more efficient than the original gLASSO algorithm of Friedman, Hastie and Tibshirani (2008). The efficiency is attributed to P-gLASSO's flexibility with initial values, whereas gLASSO operates with a strict choice of initial $\hat{\Omega}$ ($\overline{\Sigma}^{-1}$ in case of Eq. (15)). In Algorithm 1, the estimate $\hat{\Omega}$ from the past iteration serves as a warm start for the next iteration, so that we do not have to redo the entire paths from $\overline{\Sigma}^{-1}$ to $\hat{\Omega}$. We can further reduce the computation cost by harnessing the banded sparse structure of Ω in

Fig. 4. In Algorithm 2, we provide a modified P-gLASSO algorithm designed for the banded sparsity. The modified algorithm reduces the size of the LASSO sub-problem from $2T$ to $2d_{\text{cross}} + 2d_{\text{auto}}$ and the computational cost of a P-gLASSO iteration from $O(T^4 + T^3N)$ to $O(T((d_{\text{cross}} + d_{\text{auto}})^3 + (d_{\text{cross}} + d_{\text{auto}})^2N))$.

Algorithm 2 Modified P-gLASSO algorithm

Input:

$\Omega_{\text{init}}, \Sigma_{\text{init}} \in \mathbb{R}^{P \times P}$: initial values, $\Sigma_{\text{init}} = (\Omega_{\text{init}})^{-1}$
 $\bar{\Sigma} \in \mathbb{R}^{P \times P}$: sample covariance matrix of a P -variate random variable
 $\Lambda \in [0, \infty]^{P \times P}$: sparsity penalty matrix
 $\text{iter}_{\text{max}} \in \mathbb{N}_+$: maximum iteration
 $\text{ths} \in \mathbb{R}_+$: threshold for convergence

Output: Ω and $\Sigma = \Omega^{-1}$ which solves Eq. (15)

Initialization:

1: $\Sigma \leftarrow \Sigma_{\text{init}}, \Omega \leftarrow \Omega_{\text{init}}$

Iteration:

2: **for** iter in 1: max_{iter} **do**

3: $\Sigma_{\text{last}} \leftarrow \Sigma, \Omega_{\text{last}} \leftarrow \Omega$

4: **for** p in 1: P **do**

5: D_k : the collection of q 's in $[P]$ s.t. $q \neq p$ and $\Lambda_{p,q} < \infty$

6: I_p : the collection of q 's in 1: P s.t. $q \neq p$ and $\Lambda_{p,q} = \infty$

7: (We notate the submatrix of a matrix $A \in \mathbb{R}^{P \times P}$ of rows in $I \subset [d]$ and columns in $J \subset [P]$ by A_{IJ} . We moreover use $-p$ as a notation for $[d] \setminus \{p\}$ when it is used as a subscript of A .)

8: $W = (\Omega_{-p,-p})^{-1}$ can be easily calculated by $\Sigma_{-p,-p} - \Sigma_{-p,p}\Sigma_{-p,p}/\Sigma_{p,p}$

9: $\Sigma_{p,p} \leftarrow \bar{\Sigma}_{p,p} + \Lambda_{p,p}$

10: $\Omega_{p,D_p}, \Omega_{D_p,p} \leftarrow \text{LASSO}(\Sigma_{p,p} \cdot W_{D_p,D_p}, -\bar{\Sigma}_{p,D_p}, \Lambda_{p,D_p})$ with an initial value Ω_{p,D_p} .

11: $\Omega_{p,I_p}, \Omega_{I_p,p} \leftarrow \mathbf{0}$

12: $\Sigma_{p,-p}, \Sigma_{-p,p} \leftarrow -W_{:,D_p} \Omega_{D_p,p} \Sigma_{p,p}$

13: $\Omega_{p,p} \leftarrow (1 - \Omega_{p,D_p} \Sigma_{D_p,p}) / \Sigma_{p,p}$

14: $\Sigma_{-p,-p} = W + \Sigma_{-p,p} \Sigma_{-p,p} / \Sigma_{p,p}$

15: **end for**

16: **if** $\max(|\Sigma - \Sigma_{\text{last}}|) < \text{ths}$ **then**

17: **break**

18: **end if**

19: **end for**

B.2. Sensitivity of the Algorithm to Initial Values. We tested the sensitivity of Algorithm 1 to the factor loadings $\beta_k^{(t)}$ initial values, under the simulation setting in Section 3.1. Given a simulated dataset, we ran Algorithm 1 starting from 1000 different sets of initial values for $\beta_k^{(t)} \in \mathbb{R}^{d_k}$ were randomly sampled independently across $k = 1, 2$ and $t \in [T]$ from a standard d_k -dimensional multivariate Gaussian distribution. Fig. B.1 shows the LaDynS estimates $\hat{\Omega}_{12}$ from Algorithm 1 for the same dataset and three sets of initial values. Although the three $\hat{\Omega}_{12}$'s have different values, they yield similar inference for lead-lag relationships between the two time-series. The most obvious differences are the signs of the estimated precision entries, but these have no implication on lead-lag inferences because the signs of the factor loadings $\beta_k^{(t)}$ and the latent precision matrix Ω are not identifiable. Fig. B.2a confirms that the lead-lag inferences are consistent with the simulation setting in Section 3.1 and that the inferential uncertainty in Fig. B.2b is small compared to the size of the effect in Fig. B.2a.

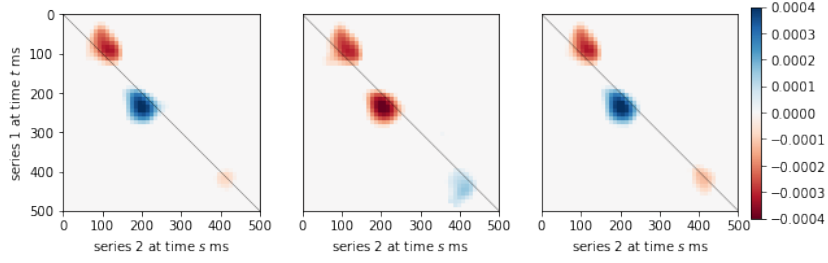


Fig B.1: LaDynS estimates $\hat{\Omega}_{12}$ by Algorithm 1 for a given simulated dataset and three sets of initial values for $\beta_k^{(t)}$'s. The dataset was generated as described in Section 3.1, with Fig. 5a showing the true Ω_{12} . The three estimates $\hat{\Omega}_{12}$ are similar and close to Ω_{12} , suggesting that Algorithm 1 is not overly sensitive to initial values.

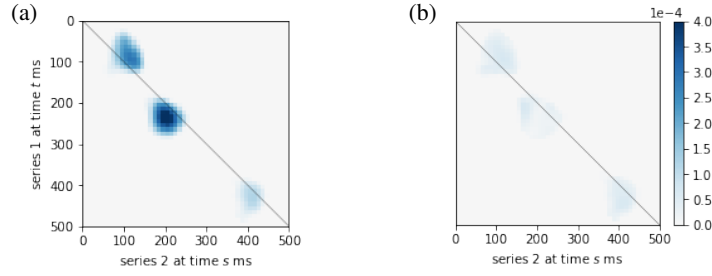


Fig B.2: (a) Mean and (b) entry-wise standard deviation of 1000 repeat Ω_{12} obtained by Algorithm 1 for a fixed dataset and 1000 different sets of initial $\beta_k^{(t)}$'s. We used the same dataset as in Fig. B.1. The mean estimated lead-lag effects in (a) are close to the true effects in Fig. 5(a), and the inferential uncertainty in (b) is small compared to the size of the effects in (a).

Next, we checked that the estimated factor loadings were similar across the 1000 runs of Algorithm 1 with different initial values. Because they are $(d_1 + d_2) \times T$ -dimensional, we projected them on an arbitrary 2-dimensional subspace to visualize them. Fig. B.3 shows the projected initial and final values of the factor loadings across the 1000 runs of Algorithm 1. The initial values in Fig. B.3a are randomly distributed, by design, and converge to a distribution that is consistent across repeat simulations. Fig. B.3 is consistent with our observation in Fig. B.1 that the main source of the sensitivity to initial values are the signs of the precision entries in the three epochs of lead-lag relationships. Indeed, because the signs for each epoch are not identifiable, we expect $2^3 = 8$ local minima in Eq. (14), where each minimum corresponds to a set of possible signs for the three epochs. Therefore, we expect see at most 8 clusters in Fig. B.3b (at most because clusters can overlap one another). The fitted factor loadings are not exactly equal within a cluster across repeat simulations because we optimize the likelihood Eq. (14) numerically.

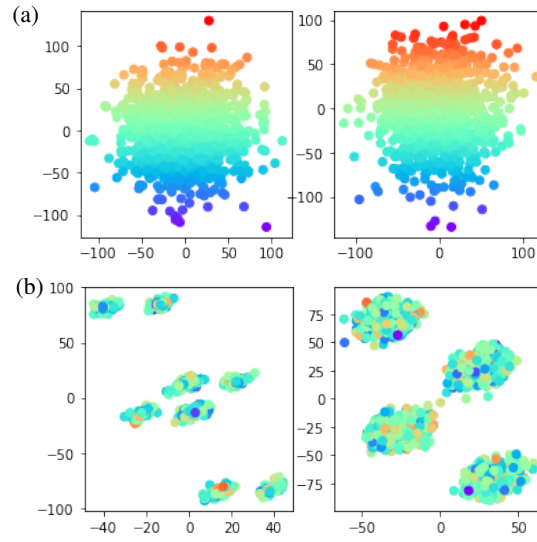


Fig B.3: Scatterplots of 2D random projections of (a) 1000 different initial values of $\beta_k^{(t)}$'s and (b) corresponding fitted values after applying Algorithm 1 to the dataset used in Fig. B.1. The same projections were used for final and initial values. The left and right panels correspond to the projected β_1 and β_2 , respectively. The distributions of initial values are random, by design. Fitted values converge to the same locations, further confirming that Algorithm 1 is not sensitive to initial values.

APPENDIX C: SUPPLEMENTARY RESULTS ON SIMULATED DATA

C.1. Simulated datasets with amplitude correlation but no coherence. Here we illustrate that LaDynS can discover lead-lag relationships in amplitude where frequency-domain analyses based on coherence or phase locking cannot.

We modified the simulation setting of Section 3.1 to generate time series that have lead-lag relationships in amplitude but no coherence. We generated two sets of multi-variate LFP time series using Eq. (27), except that L_1 and L_2 were randomly phase-shifted from $L_{0,j}$:

$$(C.1) \quad L_k^{(t)} = \sum_{j=1}^3 \beta_{kj} \cdot e^{i\omega_{kj}} \cdot L_{0,j}^{(t-\tau_{kj})} + \eta_k^{(t)}, \text{ for } k = 1, 2,$$

where i in the exponential function is the complex unit, and ω_{kj} is a random phase shift sampled from Uniform distribution $U[0, 2\pi]$. One simulation dataset consisted of 1000 trials, and the coherence and amplitude correlation at $f_0 = 18$ Hz was studied. We filtered the simulated LFPs at frequency f_0 as in Section 3.1. Let $(\tilde{X}_1^{(t)}, \tilde{X}_2^{(t)})$ be the filtered data downsampled to 100 Hz; these data are complex-variate, of which the arguments and absolute values are the oscillatory phases and amplitudes of $L_k^{(t)}$ at frequency f_0 , for $k = 1, 2$ respectively. That is, the beta power envelope $X_k^{(t)}$ is the absolute value of $\tilde{X}_k^{(t)}$. In Section 3.3, we recovered the true latent factor $(Z_1^{(t)}, Z_2^{(t)})$ as

$$Z_k^{(t)} = w_k^{(t)\top} X_k^{(t)} \text{ for } t = 1, \dots, T, \quad k = 1, 2,$$

based on Eq. (12) and known factor loadings $(\beta_1^{(t)}, \beta_2^{(t)})$. Here we also define

$$\tilde{Z}_k^{(t)} = w_k^{(t)\top} \tilde{X}_k^{(t)} \text{ for } t = 1, \dots, T, \quad k = 1, 2.$$

The cross-coherence $C_{12}^{(t,s)}$ between $\tilde{Z}_1^{(t)}$ and $\tilde{Z}_2^{(s)}$ is the population coherence between $\tilde{X}_1^{(t)}$ and $\tilde{X}_2^{(s)}$, whereas the cross-correlation $\Sigma_{12}^{(t,s)}$ between $Z_1^{(t)}$ and $Z_2^{(s)}$ is the population amplitude correlation. Fig. C.1 shows the estimates of C_{12} , Σ_{12} and the amplitude cross-precision Ω_{12} based on the average of 200 repeats, as in Section 3.3. We can verify that there is no cross-coherence between the two time series and that the amplitude cross-correlation is as in Section 3.1.

To verify that LaDynS can estimate the lead-lag relationships in amplitude, we applied LaDynS to a simulated beta power envelope dataset $(X_1^{(t)}, X_2^{(t)})$. Fig. C.2 shows the LaDynS estimate of Ω_{12} . Although there is no coherence between the two time series, the LaDynS estimate recovers the true cross-precision in Fig. C.1c, when coherence-based frequency-domain methods cannot find a significant coherence at any pair of time points.

C.2. Analysis of simulated datasets with known canonical correlation matrix. To further examine the properties of LaDynS and associated inference procedures, we present the results of another simulation study. One simulated dataset consisted of $N = 1000$ i.i.d. vector time-series X_1 and X_2 of dimensions $d_1 = d_2 = 25$ and durations $T = 50$, simulated from Eqs. (7) and (8). The latent time series Z_1 and Z_2 in Eqs. (7) and (8) had zero mean vectors and covariance matrix $\Sigma = \Omega^{-1}$, with

$$(C.2) \quad \Omega = \begin{bmatrix} (\Sigma_{0,1} + \lambda I_T)^{-1} & \Omega_{12} \\ \Omega_{12}^\top & (\Sigma_{0,2} + \lambda I_T)^{-1} \end{bmatrix},$$

where Ω_{12} was the cross-precision matrix of interest. The elements of the auto-precision matrices were simulated from the squared exponential function:

$$(C.3) \quad \Sigma_{0,k}^{(t,s)} = \exp(-c_{0,k}(t-s)^2), \quad k = 1, 2$$

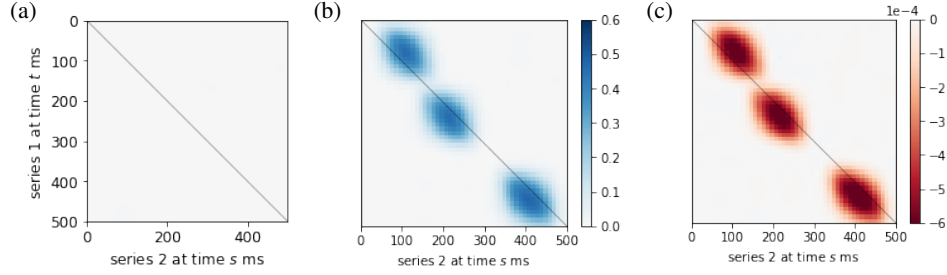


Fig C.1: (a) **Cross-coherence matrix** C_{12} , (b) **cross-covariance matrix** Σ_{12} and (c) **cross-precision matrix** Ω_{12} of two latent time-series simulated as in Appendix C.1. Lead-lag relationships between amplitudes of the simulated time series are present, but there is no coherence between their phases.

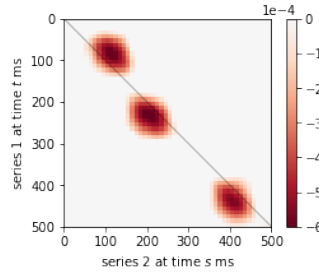


Fig C.2: **LaDynS cross-precision matrix estimate** $\hat{\Omega}_{12}$ to the simulated data without cross-coherence. LaDynS can discover lead-lag relationships in amplitude where frequency-domain analyses based on coherence or phase locking cannot.

with $c_{0,1} = 0.148$ and $c_{0,2} = 0.163$ chosen to match the LFPs autocorrelations in the experimental dataset. The diagonal regularizer λI_T was added to ensure that $\Sigma_{0,1}$ and $\Sigma_{0,2}$ were invertible, and we set $\lambda = 1$. For Ω_{12} , we considered the connectivity scenario depicted in Fig. C.3a, where the two latent times series connected in three epochs, the first with no latency, the second with series 2 preceding series 1, and the third with series 1 preceding series 2. We accordingly set the cross-precision matrix elements to

$$(C.4) \quad \Omega_{12}^{(t,s)} = \begin{cases} -r, & \text{if } (t,s) \text{ is colored red,} \\ 0, & \text{elsewhere,} \end{cases}$$

where r measured the intensity of the connection. Finally, we rescaled Σ to have diagonal elements equal to one.

Once the latent time series Z_1 and Z_2 were generated, we simulated a pair of observed time series according to

$$(C.5) \quad X_k^{(t)} = Y_k^{(t)} - \beta_k^{(t)} w_k^{(t)\top} \left(Y_k^{(t)} - \mathbb{E}[Y_k^{(t)}] \right) + \beta_k^{(t)} Z_k^{(t)},$$

for $k = 1, 2$ and $t = 1, \dots, T$, where $Y_1^{(t)}$ and $Y_2^{(t)}$ were uncorrelated baseline time series, $\beta_k^{(t)}$ were factor loadings that change smoothly over time, $w_k^{(t)}$ were canonical weights that satisfy the relationship with $\beta_k^{(t)}$ in Eq. (11), and $\mathbb{E}[Y_k^{(t)}]$ was the mean of $Y_k^{(t)}$, for $k = 1, 2$. We subtracted $\beta_k^{(t)} w_k^{(t)\top} \left(Y_k^{(t)} - \mathbb{E}[Y_k^{(t)}] \right)$ to ensure that $X_k^{(t)}$ had canonical correlation matrix Σ and the same mean as $Y_k^{(t)}$. Note that, unlike in Section 3.1, the canonical correlation

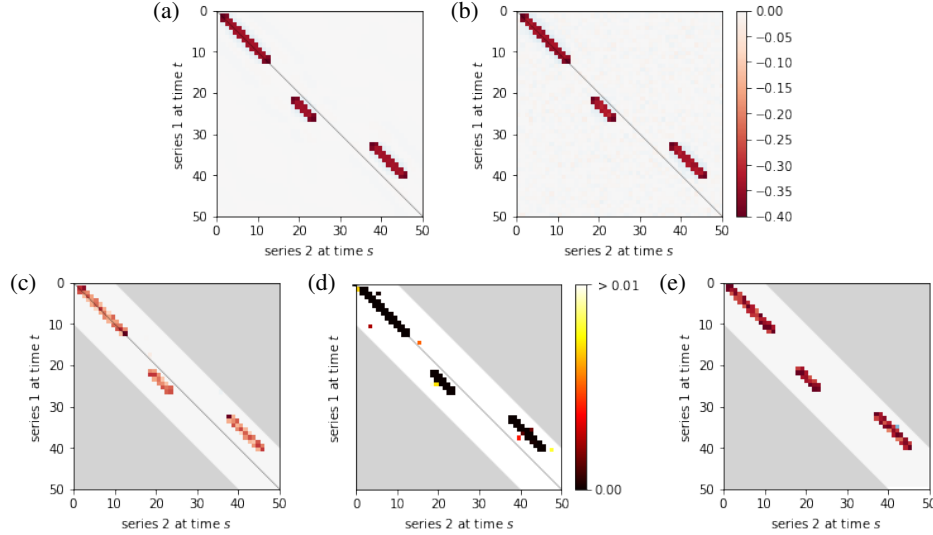


Fig C.3: Output and inference of LaDynS applied to one simulated dataset from the La-DynS model. (a) True cross-precision matrix Ω_{12} , for the connectivity scenario described in Appendix C.2 with $r = 0.4$. (b) Average over 60 simulation datasets of LaDynS de-sparsified precision estimates $\tilde{\Omega}_{12}$. There is a good match to the true Ω_{12} in (a). (c) Cross-precision estimate $\hat{\Omega}_{12}$ for one simulated dataset. It matches (a) up to random error. (d) Permutation bootstrap p-values for the de-sparsified estimate $\tilde{\Omega}_{12}$. (e) Discovered non-zero cross-precision estimates by the BH procedure at nominal FDR 5%. The cluster-wise p-values of the three discovered clusters by the excursion test were all smaller than 0.5%. All the panels but (d) share the same color bar in (b).

matrix was known exactly. We took $Y_1^{(t)}$ and $Y_2^{(t)}$ to be the two multivariate time-series of neural recordings analyzed in Section 4, which we permuted to remove all cross-correlations. To reduce temporal auto-correlations, we added space-correlated white noise to the baseline time series. The amount of noise was set to be comparable to the diagonal regularization λI_T introduced in Eq. (C.2). Finally we set $\beta_k \in \mathbb{R}^{d_k \times T}$ to be the factor loadings estimated in Section 4. The resulting latent time series $\beta_k^{(t)} Z_k^{(t)}$ and noise baseline vector $Y_k^{(t)}$ in Eq. (C.5) had comparable scales and auto-correlations by construction, for $k = 1, 2$, to the experimental data in Section 4.

LaDynS estimation details. For this simulation, we did not need to regularize the diagonal of Ω , because the simulated time series were not smooth, and the resulting $\hat{\Sigma}$ was invertible without the regularization. Hence we set $\lambda_{\text{diag}} = 0$. The other hyperparameters were set to $d_{\text{auto}} = d_{\text{cross}} = 10$, and $\lambda_{\text{auto}} = 0$. The penalty on the cross-correlation elements, λ_{cross} , was automatically tuned at every repeat of simulation to control false discoveries (see Section 2.3).

Results. Figure C.3c displays the LaDynS cross precision estimate $\hat{\Omega}_{12}$ fitted to one dataset simulated under the connectivity scenario depicted in Fig. C.3a, with connection strength $r = 0.4$ in Eq. (C.4). Figure C.3d shows the permutation bootstrap p-values for the entries of the desparsified cross-precision estimate $\tilde{\Omega}_{12}$ (Eq. (19) with permutation bootstrap simulation size $B = 200$; see Section 2.4). Small p-values concentrate near the locations of true non-zero cross-precision entries and are otherwise scattered randomly. We applied first the BH procedure with target FDR 5% (Section 2.4) and subsequently the excursion test at the 5% significance level to all discovered clusters. The significant clusters ($p < 0.005$) are plotted

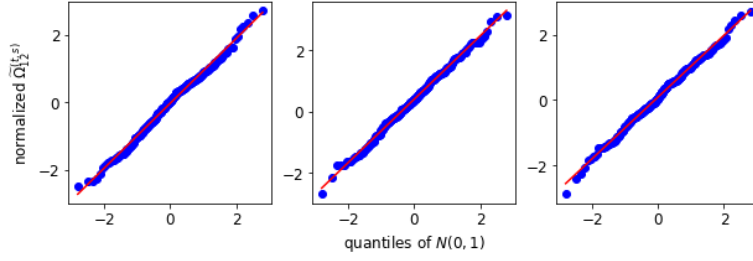


Fig C.4: **Null distributions of three representative entries of $\tilde{\Omega}_{12}^{(t,s)} / \sqrt{\widehat{\text{Var}}[\tilde{\Omega}_{12}^{(t,s)}]}$** obtained from $R = 60$ simulated datasets (Appendix C.2), compared to the standard Gaussian distribution via QQ-plots. There is good agreement.

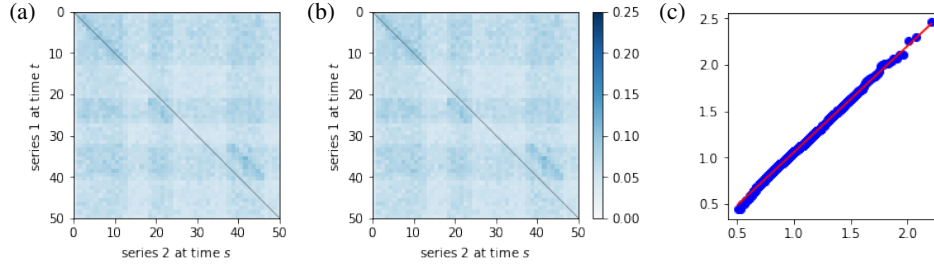


Fig C.5: **Standard deviations of desparsified precision elements.** Variance obtained (a) from samples from the ground-truth generative multiset pCCA model and (b) from permutation bootstrapped samples. (c) F-statistics of ratios between the two variances for null entries of Ω_{12} , showing good agreement.

in Fig. C.3e. They match approximately the true clusters in Fig. C.3a, although they exhibit random variability. To average this random variability out, we estimated Ω_{12} for each of 60 simulated datasets, and plotted their average in Fig. C.3b. The average LaDynS estimate is a close match to the true cross-precision matrix in Fig. C.3a.

Normal approximation for the p-values in Eq. (19). We investigated the validity of the Normal assumption by comparing the empirical distribution of $R = 60$ repeat estimates $\tilde{\Omega}_{12}^{(t,s)} / \sqrt{\widehat{\text{Var}}[\tilde{\Omega}_{12}^{(t,s)}]}$ (Eq. (18)) to the standard normal distribution using QQ-plots. Fig. C.4 shows QQ-plots for three randomly chosen representative time pairs (t, s) that are such that $\Omega_{12}^{(t,s)} = 0$, which validates the normal assumption. We further checked the validity of the permutation bootstrap variance estimates $\widehat{\text{Var}}[\tilde{\Omega}_{12}^{(t,s)}]$, shown in Fig. C.5b, by comparing them to the empirical variances of $R = 60$ estimates $\tilde{\Omega}_{12}^{(t,s)}$, shown in Fig. C.5a. There is good agreement for the entries that have precision value zero, $\Omega_{12}^{(t,s)} = 0$. Fig. C.5c further displays the Q-Q plot of the repeat ratios of permutation bootstrap over empirical estimates of $\text{Var}[\Omega_{12}^{(t,s)}]$ for these entries, with $F(B - 1, R - 1)$ being the reference distribution. The good agreement suggests that the bootstrap estimate of $\text{Var}[\Omega_{12}^{(t,s)}]$ is reliable.

FDR control. Fig. C.6 shows that estimated and target FDR values match for a range of connection strengths (r in Eq. (C.4)). In addition, the FNR is very low for target FDRs larger than 2%.

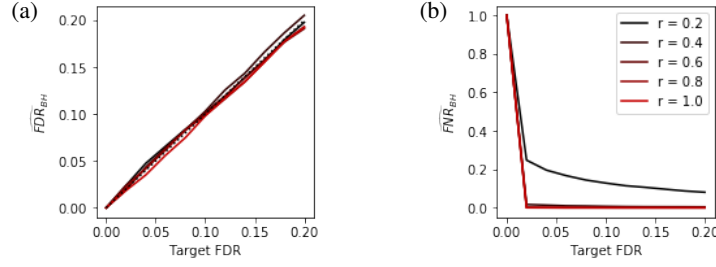


Fig C.6: **False Discovery Rate control for LaDynS' inference.** (a) *Estimated false discovery rate* and (b) *false non-discovery rate* for target $FDR \in [0, 20]\%$, under the connectivity scenario in Fig. C.3a, for connectivity intensities $r = 0.2, 0.4, 0.6, 0.8$ and 1.0 in Eq. (C.4). The dotted line is a $(0,1)$ line.

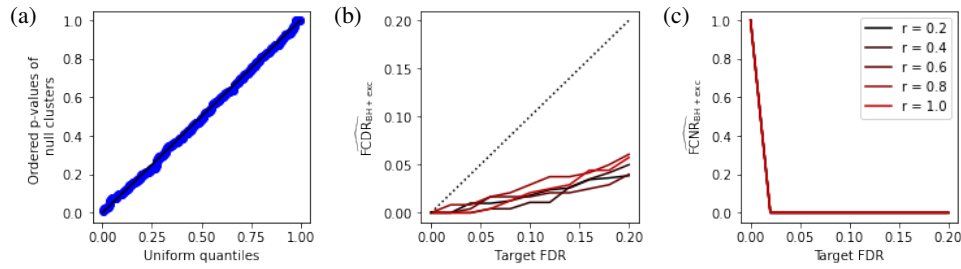


Fig C.7: **Performance of cluster-wise inference after excursion test.** (a) *Q-Q plot of excursion test p-values from null clusters versus Uniform[0, 1] distribution, as expected of a valid test.* (b) *false cluster discovery rates* and (c) *false cluster non-discovery rate of BH at target FDR 10% followed by excursion test at significance level $\alpha \in [0, 0.10]$ to identify non-zero partial correlations, under the connectivity scenario in Fig. 5a, for the simulated range of connectivity intensities.*

Excursion test. The next step was to apply the excursion test to each cluster discovered by the BH procedure at target FDR 5%. As a check on the validity of this test, Fig. C.7a shows the quantiles of null p-values versus the theoretical quantiles of the uniform distribution on $[0, 1]$. They match perfectly so the excursion test is reliable. Finally, Figs. C.7b and C.7c display the cluster-wise FDR and FNR (FCDR and FCNR) for the BH procedure followed by the excursion test. The estimated FCDRs (Fig. C.7b) are small throughout the tested range of nominal FDR values and connectivity intensities. The estimated FCNRs (Fig. C.7c) are zero for nominal FDRs greater than 2%, which means that all connectivity epochs in Fig. C.3a were discovered by our methods in the simulated dataset.

APPENDIX D: SUPPLEMENTARY FIGURES FOR THE EXPERIMENTAL DATA
ANALYSIS IN SECTION 4

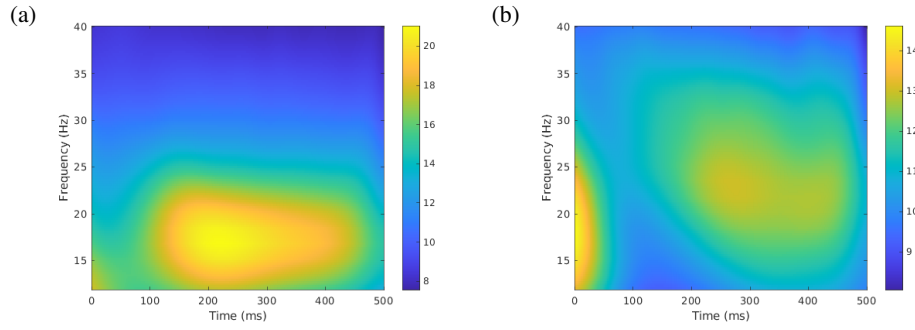


Fig D.1: Averaged spectrograms across trials and electrodes in (a) V4 and (b) PFC as functions of experimental time, cropped at frequency between 12 Hz and 40 Hz to focus on the beta band oscillations.

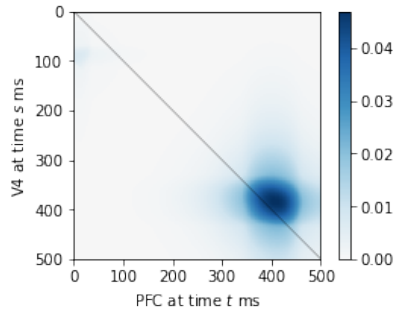


Fig D.2: Latent cross-correlation matrix estimate $\hat{\Sigma}_{12}$.

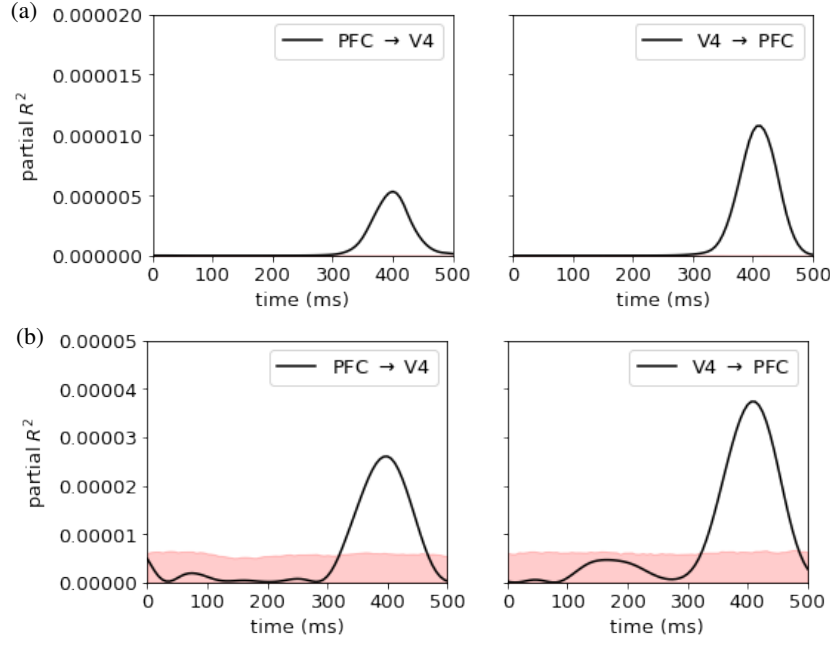


Fig D.3: **Estimated partial R^2 from locally stationary state-space model based on (a) the LaDyns precision estimate $\hat{\Omega}$ and (b) desparsified estimate $\tilde{\Omega}$ for $V4 \rightarrow PFC$ and $PFC \rightarrow V4$.** The pink shaded areas are the 95th percentiles of null partial R^2 under independence between V4 and PFC.

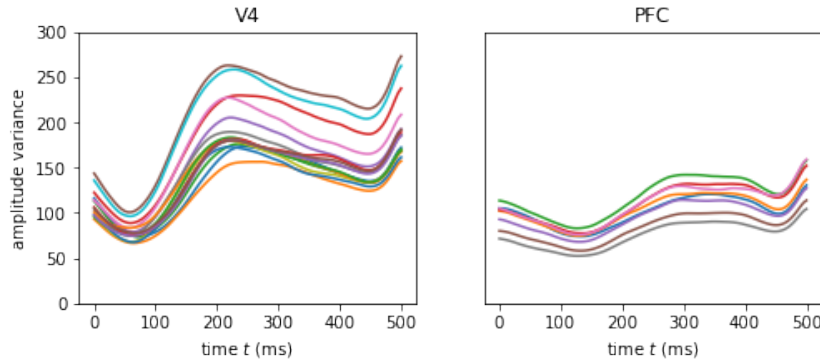


Fig D.4: **Estimated variances of beta amplitudes at active electrodes in V4 and PFC as functions of time.** The active electrodes were those with factor loading values larger than 75% of the maximal value at experimental time 400 ms (Fig. 12 shows the factor loadings at 400 ms over the electrode arrays). There were 19 active electrodes in V4 and 16 in PFC.